

Perspectives on Electron Transfer Kinetics Across Graphene-Family Nanomaterials and Interplay of Electronic Structure with Defects and Quantum Capacitance

Sanju Gupta^{a,b,c,d,*} Magdalena Narajczyk^e, Mirosław Sawczak^f, Robert Bogdanowicz^{a,b}

^a Department of Metrology and Optoelectronics, Faculty of Electronics, Telecommunication and Informatics, Gdansk University of Technology, Narutowicza Str. 11/12, 80-233 Gdansk, Poland

^b Advanced Materials Center, Gdansk University of Technology, 80-233 Gdansk, Poland

^c Department of Physics, Pennsylvania State University, University Park, PA 16802 (USA)

^d Department of Physics and Astronomy, University of Georgia, Athens, GA 30602 (USA)

^e Faculty of Biology, University of Gdansk, Wita Stwosza 59, 80-308 Gdansk, Poland

^f The Szewalski Institute of Fluid-Flow Machinery, Polish Academy of Sciences, Fiszerza 14, 80-231 Gdansk, Poland

*email: sgup77@gmail.com. Alternative: sangupta@pg.edu.pl

ABSTRACT

This perspective presents a combined experimental-theory investigation of the mechanistic outer-sphere electron transfer (OS-ET) kinetics in an adiabatic regime for a cornerstone electrochemical reaction, fundamental to efficient energy interconversion as in electrochemical double layer supercapacitors, across graphene-family nanomaterials (GFNs) ranging from pristine graphene to nitrogen-doped graphene aerogel and the novel laser-induced graphene. Using scanning electrochemical microscopy (SECM) operating in feedback mode and co-located spectroscopy, the ET rate constant, k^0 (or k_{ET} , cm/s) was quantified while imaging electroactivity of potassium hexacyanoferrate (III/IV) [$Fe(CN)_6^{4-/3-}$] or ferrocene methanol [Fc^0/Fc^+] redox probe yielding unexpected trends. We examined factors affecting the kinetic rate constant, rationalized through a physical model and parameterized using density functional theory by incorporating defects and dopants. We attributed the improved kinetic rates (0.01–0.1 via SECM) compared with ensemble-averaged method (0.001–0.01 cm/s) to point-like topological defects in basal plane (number density $\sim 10^{12}/\text{cm}^2$), oxygen functional groups (C/O ratio: 4:1–12:1), nitrogen doping, and edge plane hydrogen-bonding sites (density: 0.1–1.0 μm^{-1}), altering the electronic structure factored into available density of states near Fermi level (–0.2–+0.2 eV), and quantum capacitance. We elucidated the ET kinetics tunability by engineering the electronic band structure, varying electrode potential, and morphological diversity.

Keywords: GFNs; laser-induced graphene; SECM; electron transfer; electroactivity; quantum capacitance; DFT, physical model.

Corresponding author. E-mail: sgup77@gmail.com (S. Gupta). Alternative: sangupta@pg.edu.pl

1. Introduction

Since the inception of atomic-thin monolayer graphene from graphite exfoliation almost two decades ago, it has gone considerable evolution and inspired fundamental discoveries as well as multitude of applications from electronics and photonics to life science. Graphene monolayer consists of sp^2 -bonded carbon (sp^2C) atoms organized in a two-dimensional (2D) honeycomb or hexagonal lattice, where each carbon atom shares with three in-plane σ -bonds and an out-of-plane π -bond (average interatomic distance = 1.42 Å) [1]. As a result, a family of graphene-related nanomaterials have been intensely investigated giving rise to their outstanding chemical and physical properties (*e.g.*, charge carrier mobility, mechanical stiffness, optical transparency, electrochemical activity, thermal and electronic conductivity) attributed to high specific surface area (*ca.* $\sim 2,630\text{ m}^2\text{g}^{-1}$) and peculiar atomic structure [2]. Graphene derivatives including graphene oxide (GO) and reduced form, rGO produced using chemical (CerGO) and electrochemical reduction (ErGO), thermal (rGO_{th}) and hydrothermal decomposition (rGO_{HT}) are equally promising due to presence of surface functional groups on their basal plane and edge sites [3]. It has been found that the chemical structure and composition of the rGO_{th} produced thermally and hydrothermally rGO_{HT} were comparable in their chemical structure. Thus, graphene-based electrodes has been heralded as promising materials for analytical and industrial electrochemistry [4, 5] as in biochemical sensors [6, 7, 8, 9, 10], solar cells [11], water purification [12], gas separation [13, 14], electrocatalytic platforms [15] and energy conversion and storage systems [16, 17, 18, 19] ascribed to facile production, easy processability, scalability, and cost effectiveness [20, 21, 22]. Among the assortment of these graphene-family nanomaterials (GFNs), we expand the scope by introducing laser-induced graphene (LIG) produced by direct laser scribing of carbonaceous precursors [23, 24]. Specifically, it is produced through a single-step scalable, patternable (from nano-micro to macro dimension), industrially deployable, and cost-effective infrared CO₂ laser manufacturing techniques inducing photochemical and thermal conversion of commercial polyimide (PI) into a three-dimensional (3D) interconnected network of multilayer graphene sheets forming an intriguing porous graphemic film in ambient atmosphere [25, 26]. The photothermally converted sp^2 -carbon (sp^2C) atoms are produced from sp^3 -carbon (sp^3C) atoms in PI film forming laser-induced ‘porous’ graphene (LIPG, hereon) that contains pentagon-heptagon coordinated rings as topological structures namely, Stone-Wales defects [27]. LIPG has high electrical conductivity of graphene, large surface area, resistance to strain and chemical



corrosion, and it can be functionalized to catalyze chemical and electrochemical reactions. Therefore, despite LIPG being relatively new, use of 2D graphene in 3D superstructures has inspired fundamental electrochemistry as in this work as well as applications in flexible/foldable electronics, biochemical sensors, environmental engineering, energy storage micro-supercapacitors (MSCs) and other favorable customizable devices [28, 29, 30,31,32]. In this context, laser-based approaches for synthesizing, modifying, reducing, and assembling graphene related electrodes and devices are in enormous demand.

The efficient performance of graphene-family nanomaterial (GFN) electrodes as electrochemical capacitors (or supercapacitors) depends upon their chemical composition and electronic structure. These factors influence the kinetics of dynamic (electrified) interfacial processes by affecting energy storage through the formation of an electric double layer (EDL) at the electrode-electrolyte interface [33,34,35, 36]. There are major strategies to improve the areal EDL capacitance for GFNs include [37, 38]: 1) creating topological defects or N doping; 2) increasing specific surface area to enhance active area of the EDL; and 3) optimizing pore structure to allow desolvated ions to penetrate and reducing charge separation distance of the EDL thereby enhanced energy storage capacity. Thus, an in-depth mechanistic understanding through which the topological point defects and dopant affect the EDL call for strategic design of diversified GFN electrode materials. A persistent interest of nanocarbons arises due to structural polymorphism, chemical stability, relative inert electrochemistry *albeit* rich surface chemistry, and wide operational potential window in organic and ionic liquid electrolytes becomes the focus of modern electrochemical technologies with less exploration on fundamental electrochemical investigations addressed in this study.

Electrochemistry offers unique possibilities to modify kinetics of redox reactions at electrode-electrolyte interface by changing the morphology and electronic structure of electrode and varying potential thereby playing key roles in various processes relevant to electrochemical energy, biology, and geochemistry. The advanced electrochemical electrodes for sustainable alternative energy sources based on conducting graphene or graphene supported on metal rely on different mechanisms of energy storage and conversion, which ranges from surface ion adsorption (supercapacitive) afore mentioned to pseudocapacitive intercalation and Faradaic redox processes [39, 40, 41]. Specifically, the research related to heterogeneous electron transfer (ET) kinetic reaction of complex ions in solution is fueled by experimental data related to graphene electrodes

that indicate a significant change occurring in electroactivity due to various sources including atomic scale defects [42, 43] such as mono- and di-vacancies [44], oxygen-containing functional groups [45], nitrogen doping [46, 47, 48], and abundant edge sites [49, 50], disrupting intrinsic sp^2C conjugation in addition to nanoscale corrugations within graphene basal plane leading to curved topology that affects electroactivity [51, 52, 53, 54]. Generally reported in many works, the step edge plane sites were considered more electrochemically reactive than the basal plane sites while claiming relatively low or almost no basal activity of highly oriented pyrolytic graphite (HOPG)-based electrode [55, 56, 57]. As a result, it was concluded that the ET mainly occurs at the edge planes of the graphene and sides of carbon nanotube with implications on the strategic synthetic development of morphological surfaces defined by vertically aligned graphene or carbon nanowalls, graphene aerogels, and mesoporous graphene exposing the edge sites [58, 59, 60]. Moreover, it is reported that ET kinetics pertaining to such enhancement dramatically affected by observations that depend upon three significant phenomena; defects within basal plane and edge plane sites, heteroatom dopants, redox couples' mechanism (outer sphere, OS *versus* limited inner sphere, IS), and surface electronic structure, without extracting atomic level insights which remained challenging [61]. For instance, a freshly cleaved HOPG surface displayed uniform and high electrochemical response analogous to noble metal electrodes for outer-sphere redox process [62, 63]. While the activity decreased with time due to spontaneous delamination of top layer leading to aged surface from the remainder underneath layers with standard potential close to potential of zero charge [64, 65], an enhanced current at the edges from aged graphite was observed. From practical viewpoint, utilizing only edge sites appears inefficient leading to low edge to plane (E/P) sites ratio and thus, diverse structural imperfections afore mentioned should be entertained to impart electrochemical property enhancement from the whole surface area. Nevertheless, theoretical calculations predicted comparable basal and edge plane oxygen reduction reaction rate attributed to strong overlap of donor and acceptor orbitals (*adiabatic ET*) as opposed to longer separation or weak overlap (*nonadiabatic ET*) where zigzag or random protruded edges provide faster ET [66, 67, 68].

It is increasingly recognized that true understanding of complex electrochemical reactions at atomic level is conceived by combining suitable experiments, theory, and physical modeling, the focus of this study. The development of advanced tip-based (local) electrochemical techniques such as scanning electrochemical microscopy; SECM [33, 69, 70, 71, 72] and scanning



electrochemical cell microscopy; SECCM [73], governed by well-known scanning probe microscopy methods, reveal physicochemical behavior that is far from “simple” and well-behaved from aforementioned reports inviting comprehensive discussion. The interaction is facilitated through a redox mediator rather than Van der Waals forces as in atomic force microscopy. The mediator creates a redox cycle (reaction) between the tip and the substrate (electrode) under study. Thus, depending on the nature of the substrate, the cycle is stimulated (conductive material) or suppressed (insulating material). While analytical methods and computational predictions/theoretical calculations proved to be powerful tools for revealing the key characteristics providing valuable insights [74], it is challenging to include all the effects accurately to avoid enormous computing power and experimental resources. Moreover, the electrodes high-rate performance is mostly dependent on two factors: the electron transport (electrical) and mass transport (diffusion). It is increasingly recognized that a true understanding of complex electrochemical reactions at atomic level is reached by integrating experiments, theory, and physical models. Therefore, it is imperative to measure the standard ET kinetic rate constant using advanced experimental techniques and corroborate with theoretical calculations and physical model predictions. This situation has recently changed significantly due to the advances in electronic structure theory *i.e.*, density of states (DOS) determination through density functional theory (DFT) calculations and computer simulations.

The main accent of this work is to examine the mechanistic electron transfer (ET) processes across graphene-family nanomaterial (GFN) electrodes surface/interfaces that present a complex interplay between outer-sphere (OS-ET) and inner-sphere pathways in adiabatic regime, fundamentally governed by the coordination sphere's charge exchange capabilities. The determination of these mechanisms is intrinsically dependent on the spatial distribution between redox-active centers and the electrode surface, necessitating rigorous experimental validation complemented by computational analyses presented in this perspective report as well. GFNs include from pristine graphene (Gr) to graphene derivatives (GO, rGO, ErGO, CerGO) and graphene aerogels (GA, NGA) alongside novel laser-induced “porous” graphene (LIPG) to establish quantitative *structure* (morphology, lattice imperfections and DOS)–*property* (electrochemical)–(*electro*)*activity* (ET kinetic rate) relationships as well as mapping electroactivity by SECM, thereby advancing our understanding of complex electrified interfacial process. We consider the ET kinetics of ferrocene methanol (FcMeOH) predominantly operates



through outer-sphere electron transfer (OS-ET) mechanism, maintaining consistent kinetics across diverse surface modifications and exhibiting reduced surface chemistry dependence [75], in contrast to Ferri/Ferro $[\text{Fe}(\text{CN})_6]^{4-/3-}$ redox couple system that exemplifies characteristic inner-sphere electron transfer behavior, demonstrating pronounced sensitivity to surface chemistry and oxide functionalization states [76]. Here we also discussed briefly the extent of adiabatic versus non-adiabatic regime to the most elementary electrochemical redox reaction to provide aspects on electronic structure control of electrochemistry for GFNs.

To the best of our knowledge, the current study provides an unprecedented, detailed account of ET kinetics using traditional ensemble averaged (macroelectrode) and localized SECM (microelectrode) configurations. The order of magnitude difference in unexpected experimental trends of ET observed for GFN electrodes having diverse morphology, varied chemical composition invoking engineered electronic structure, is combined with discussion related to Gerischer–Marcus physical model as to how the energy band alignment of electrode and redox electrolyte wavefunction improve the performance. It is ascertained that the electroactivity of graphene-based electrodes largely depended on factors including topological point defects, functional groups and nitrogen dopant inducting differential electron density of states near the Fermi level significantly influencing the quantum capacitance connected in series with the Helmholtz capacitance further improving the total interfacial capacitance. Comprehensive analysis provides greater insights into ET mechanisms resulting from complex interactions between topological point defects, surface redox chemistry, morphological diversity, electronic properties factored in the available density of states influencing quantum capacitance. The ability to modulate these properties through processing parameters presents significant opportunities for optimizing electrochemical performance, even in nonaqueous electrolytes capable of high voltage operation, for the next-generation electrochemical energy and electrocatalytic applications, while emphasizing the critical importance of considering multiple mechanistic factors in next generations electrode design and characterization methodologies.

2. Experimental methods

2.1 LIPG synthesis

Kapton (PI) polymer sheets ~50 micron thick used in this work were purchased commercially from Cole Palmer (Type HN film, CatNo. WZ–08277–86, UK). They were used as

received with gentle cleaning of dust particles unless noted otherwise. Laser scribing on PI sheets was conducted with a pulsed CO₂ laser cutter system (Desktop 3D Laser Printer, Model gweike cloud RF–Laser cutter and engraver, Shandong, China): 10.6 μm wavelength of laser with pulse duration of ~50 ms. The beam size was ~160 μm giving an estimate of interlayer distance. Laser power varied from 9% to 12% of full laser power of 40 W. The laser system offers an option of controlling the scan rates from 20 to 500 mm s⁻¹ and scanning option (raster versus snake). The scan rate of 110 mm/s (or 120 mm/s) with snake option was used for all experiments. The laser system also provides an option of setting the pulses per inch or DPI (dots per inch). Here, the LIPG active electrodes used in this study were directly written using the computer-controlled CO₂ laser with pre-designed CAD files (LightBurn Beta Software, *ver.* 0.4.06).

2.2 Graphene-family nanomaterials (GFNs) synthesis

Variants of graphene electrodes such as graphene-family nanomaterials (GFNs) were synthesized using various methods provided here and referenced for details (see Fig. S1, ESI). Other than monolayer graphene prepared using classic micromechanical exfoliation method and graphene with point defects introduced using electron beam (70 keV for 50–60s), graphene oxide (GO) was used as precursor for other forms of graphene–family electrodes. GO was prepared by modified Hummer’s method followed by chemical reduction using hydrazine monohydrate producing CerGO [77, 78, 79, 80]. To synthesize GO and CerGO thin film electrodes and to determine an optimized configuration, their dispersions of 0.5 mg/mL concentration were ultrasonicated further for 30 min, drop cast onto indium tin oxide (ITO) coated glass slides of 1x4.5 cm² dimension followed by air dry and gentle thermal heating at 50–60 °C for 30–60 min. for better evaporation. For electrochemical reduction of GO producing ErGO, the GO overcoat ITO substrates were immersed in electrolyte containing 1M NaCl buffer media pH=11.85–12.0 operating in an amperometric mode at –0.9V in a conventional three-electrode electrochemical cell with Pt sheet as counter electrode and Ag/AgCl as reference electrode for 900s (15 min.). Formation of ErGO relies on the removal of oxygen-related surface functionalities and the extent of reduction was monitored using Raman spectral G band position that is red shifted by a few wavenumbers. Thermal reduction of GO at low temperature of 220 °C in quartz tube furnace with Ar flow for 1–2 h helped to produce reduced graphene, rGO_{th} [81]. As for GA and NGA, they were prepared by solvothermal/hydrothermal method (see Fig. S1, ESI) [60, 82]. The GO dispersion of 2.0 mg/mL was heated in Teflon coated autoclave at 180 °C for 20h producing



hydrogel. The dispersion was nitrogenated by adding 13.4 mL of ammonium hydroxide (NH_3OH) to 70 mL of solution (~20% ratio). This solution was heated in Teflon coated autoclave at 90 °C for 1h. The dispersions with and without nitrogen were freeze-dried for 60–72 h to remove the liquid from hydrogel and to create GA and NGA aerogel monoliths of 2-3 cm long and an inch diameter [83].

2.3 Characterization techniques

Surface Morphology and Microstructure. All the samples and electrodes were characterized using complimentary analytical techniques to reveal morphology of scanned area (particularly to identify graphene surface within micros), microstructure, and lattice vibration properties. Scanning electron microscopy (SEM) images were taken in secondary electron imaging (SEI) mode with Model Prisma E (Thermo Fisher Scientific, USA) operating at a primary electron acceleration voltage (V_{acc}) of 15 kV and constant current 45 μA with a LaB_6 filament. For transmission electron microscopy (TEM), a few flakes were distributed onto commercial carbon coated Cu grids 300 mesh (Agar and Ted Pella, CA, USA) with 2% colloidal solution and analyzed with transmission electron microscope (Model Tecnai Spirit BioTWIN at 120kV and 1 nA from LaB_6 gun with a Be specimen holder and with AMT 8 Mpixel cooled camera). TEM measurements provided nanoscale morphology and structure that help to determine interplanar spacing. Lattice vibrational spectra determined chemical composition of carbon bonding measured using a micro-Raman spectrometer (Model InVia Renishaw *plc*, Hoffman Estates, IL, USA) equipped with Ar^+ laser providing excitation wavelength $\lambda_L = 514 \text{ nm}$ ($E_L = 2.41 \text{ eV}$) or semiconducting diode laser with $\lambda_L = 532 \text{ nm}$ ($E_L = 2.33 \text{ eV}$). The reflected light is filtered using an edge filter to remove the laser excitation cutting at $\sim 100 \text{ cm}^{-1}$. The scattered light from the sample is collected in backscattering geometry with objective lens of 50x providing a spot size $\sim 1\text{--}2 \mu\text{m}$ and the laser power on the sample is maintained between $< 0.1\text{--}0.5 \text{ mW}$ (5 %) to prevent photo-thermal degradation. The Raman spectra were acquired for 90–120s depending upon the samples to maximize throughput signal. Raman spectra ranged between $100\text{--}3400 \text{ cm}^{-1}$ with spectral resolution $\sim 1 \text{ cm}^{-1}$. Each sample was analyzed at a few randomly selected points and the spectra was averaged from these measurements. The crystal structure of the obtained material was also analyzed with X-ray diffractometer (Model Philips X'pert PRO with Anton Parr HTK-1000 camera) and CuK_α radiation ($\lambda = 1.54 \text{ \AA}$) in the range $2\theta = 5^\circ\text{--}70^\circ$. The LIPG sample on PI and powder scratched from film pressed on to Si substrate were used for XRD. All other characterizations were conducted directly on LIPG film. The sheet resistance (R_s) was measured

using a Keithley four-point probe meter (Model 2400, detection limit: $1\text{G}\Omega$). The chemical structure and binding energy of LIPG was performed using Argus Omicron NanoTechnology X-ray photoelectron spectrometer (XPS) equipped with hemispherical electron analyzer with a round aperture of 4 mm. Analysis was performed at room temperature with base pressure below 1.1×10^{-9} mbar. The photoelectrons were excited by an $\text{MgK}\alpha$ X-ray anode. Measurements were taken in a constant analyzer energy mode with pass energy equal to 50 eV. To remove contamination, the surface was etched with Ar ions before the measurement. All the survey spectra were recorded in 0.5 eV step size with a pass energy of 140 eV. Elemental C1s spectra were recorded in 0.1 eV step sizes with a pass energy of 26 eV. The spectra were corrected using C1s peak (BE=284.5 eV) as reference. The data was processed in Computer Aided Surface Analysis for X-ray Photoelectron Spectroscopy, CasaXPS (ver.2.3.25) to determine carbon bonding configurations with respective binding energies.

Electrochemical. The electrochemical measurements were performed using a potentiostat-galvanostat (VMP-300, Bio-Logic, France) controlled by EC-Lab software (V11.52). Cyclic voltammetry (CV) and electrochemical impedance spectroscopy (EIS) at open circuit potential (OCP $\sim 0.1\text{V}$, within Faradaic window) were carried out in a single compartment three-electrode electrochemical setup with LIPG and other GFNs as working electrode, Ag/AgCl (3M KCl) as the reference electrode and platinum net as the counter electrode. The geometric surface area of the electrode immersed in the electrolyte was $A = 0.125\text{ cm}^2$. The electrochemical properties of LIPG electrode were taken in 0.5M Na_2SO_4 mixed with 2.5mM $[\text{Fe}(\text{CN})_6]^{4-/3-}$ redox probe. Before the electrochemical measurements, the electrolytes were deoxygenated with Ar gas to ensure full diffusion of ions onto electrodes surface. However, due to the somewhat hydrophobic nature of LIPG and monolayer graphene (unlike defective graphene and other GFNs), they were soaked in the chosen electrolyte for 3–4 h. For better electrical connection, silver paint was applied on a small area of electrode surface, that was extended with a thin conductive copper strip to connect the electrochemical workstation. To protect the contact pads from the electrolyte, Kapton PI tape was used to define the area. The CV experiments were acquired at scan rates ranged $v = 5\text{--}200\text{ mV s}^{-1}$ in potential window from -0.4 to $+0.8\text{ V}$ versus reference electrode. The *ac* EIS experiment was carried out at $E = 0\text{V}$, with ac voltage perturbation 15 mV and in frequency range from 2×10^5 to $1 \times 10^{-2}\text{ Hz}$ (200 kHz to 10 mHz), 10 points per frequency decade. All measurements were recorded at room temperature ($25\text{ }^\circ\text{C}$).



Scanning electrochemical microscopy (SECM) was performed to determine ET rate constant and gain comprehensive insights into electrode/electrolyte interfaces and to image electrochemical active sites distribution over large areas (. Feedback mode SECM measurements were carried out as detailed below (see also Fig. S3, ESI). One of the SECM setups consisted of three closed-loop piezo actuators (P625.2CD and P622.1CD, PI HERA with LVPZT Amplifier E-509 C3A, Physik Instrumente, Karlsruhe, Germany), mounted on an inverted confocal laser scanning microscope (Leica TCS SP AOBS, Leica Microsystems GmbH, Wetzlar, Germany) and a digital potentiostat (CompactStat, Ivium Technologies, Eindhoven, Netherlands) [see ref. 84 for details]. Two patch-clamp amplifiers with preamplifiers related to a bi-potentiostat for independent polarization of the sample and the SECM tip and generation/collection current measurement like the other commercial SECM system tailored to meet custom measurements, albeit yielding similar results. For either of these setups, the measurements were performed in a three-electrode cell consisting of a Pt UME (ultramicroelectrode) tip as working electrode, a Pt wire as counter electrode, and Ag/AgCl wire as reference electrode to which all potentials are referenced. The microelectrode is typically obtained by sealing Pt wire 10 μm diameter into borosilicate glass capillaries according to Kranz *et. al.*, [85]. The ratio between the radius of insulating glass r_{glass} and the tip electrode r_{tip} (RG) is ≈ 20 . If not stated otherwise, 2.5mM potassium ferro/ferricyanide in 0.5M Na_2SO_4 [or 1 mM Fc (MeOH) in 0.1M KCl] were used as electrolyte environment yielding similar results. Diffusion controlled reduction of redox probes $\text{Fe}(\text{CN})_6^{4-/3-}$ (or Fc^0/Fc^+) was carried out at +0.4V. The electrode substrate was mounted at the bottom of a Teflon cell with steel screws. The surface area contacting the electrolyte was confined to circle of 1-3 mm diameter to prevent current overflow (max. 2 μA for the equipment used). SECM voltametric measurements were conducted at scan rates: $\nu = 10, 20$, and 50 mV/s, probe approach curves with tip voltage $V_t = +0.2\text{V}$ and substrate voltage $V_s = 0\text{V}$ and imaging in probe areas of $500\text{ }\mu\text{m} \times 500\text{ }\mu\text{m}$ with 4 μm increment. The working distance (d) was adjusted by withdrawing the microelectrode by a defined distance after touching the sample electrode near the measured area (see Fig. S4, panels A and B, ESI). For the group of GFN electrodes, a commercial electrochemical workstation (Model CHI920D, CH Instruments, Austin, TX, USA) was used in cyclic voltammetry and impedance modes under similar conditions described above. The GFN sample electrodes deposited on ITO substrates were characterized in the potential range $-0.8\text{ V} - +0.8\text{ V}$ at scan rates $\nu = 10\text{--}500\text{ mV/s}$ with mixed 2.5 mM $\text{K}_4\text{Fe}(\text{CN})_6/\text{K}_3\text{Fe}(\text{CN})_6$ redox mediator in 0.5M Na_2SO_4



base electrolyte for traditional electrochemical properties. SECM measurements were conducted at scan rates: $\nu = 10, 20$ mV/s, probe approach curves with tip voltage $V_t = +0.5$ V and substrate voltage $V_s = 0$ V and imaging in probed areas of $600 \mu\text{m} \times 600 \mu\text{m}$ with $2\text{--}4 \mu\text{m}$ increment [19, 33]. SECM data analysis was carried out with the Origin software (ver. 2022b) and CHI software (ver. 12.04) using the procedure described in ESI (Electronic Supporting Information).

2.4 Computational details

DFT Parameters and periodic slab modeling. Density functional theory (DFT) calculations were performed with projector-augmented wave (PAW) pseudopotentials and Perdew–Burke–Ernzerhof (PBE) exchange–correlation functional, see also refs. [86, 87] for details. CRYSTAL17 [88] code was used to calculate the optimized geometries and electronic properties for various GFNs studied here. The advantage of CRYSTAL17 code was the use of two-dimensional slabs without the need of artificial periodicity perpendicular to the surface, typically found in other DFT codes. We used periodic restricted DFT as in our past work [35, 88] and the PBE0 non-empirical parameter-free functional form [89]. All calculations were treated using the D3 semi-empirical correction introduced by Grimme [90]. This correction improves the DFT functionals description of long-range electron correlations typically found in GFNs. All atoms described by all-electron basis sets optimized for crystalline calculations. The H, N, and C atoms treated by the pob–TZVP basis sets following Peintinger *et al.*, [91] and O atoms treated by the BSSE-corrected pob–TZVP basis set following Oliveira *et al.*, [92]. For geometry optimizations, Brillouin zone (BZ) integrations (Monkhorst–Pack grid) [93], the Fermi energy (E_F), and the density matrix calculations (Gilat grid) performed on 12×12 grid [94] were sufficient for these calculations. The electronic band structures and density of states (DOS) were obtained using the denser grids of 48×48 and 64×64 , respectively. The Fermi surface is smeared with a Gaussian of 0.005 Hartree for convergence purposes. The SCF energy threshold value for our calculations is set at 10^{-9} Hartree (default value $\sim 10^{-7}$ Hartree). The geometric stability of the final conformations is secured via post-geometry optimizations. Jmol software was used to visualize optimized geometries [16, 35, 60, 95]. Graphene is modeled as two-dimensional hexagonal lattice using the (4×4) supercell with 32 carbon atoms. The graphene calculated lattice constant is 2.445 \AA , close to the experimentally measured value for graphite (2.46 \AA). Atoms (C, N, O, and H) described by Gaussian basis sets developed by Peintinger *et al.*, [91] using the original triple- ζ for valence plus single polarization function basis sets [96, 97]. Defects on graphene support were modeled using



“ghost” massless atoms in the lattice, which share the same basis set as the original carbon atoms. Here, the ghost atoms were placed at the center of the supercell and the defect is periodically repeated using translational symmetry vectors. Furthermore, the DOS obtained through these DFT calculations for various GFNs (*e.g.*, Gr, Gr_{def}, GO, rGO) were used in theoretical models including other factors for k_{ET} predictions.

3. Results and Discussion

3.1 LIPG fabrication

The discovery of laser-induced “porous” graphene from PI carbon source is considered disruptive technology which is paving way for their simple design, environmental friendliness, programmable compositions and controllable morphologies over traditional graphene as in Fig. 1 illustration (panel a) [25, 26, 98, 99, 100]. Thus far, commercial PI is an ideal precursor by providing the carbon source containing aromatic (cyclic) and imide (NH²⁻) repeat units, as opposed to aliphatic chain polymers, likely to undergo depolymerization at laser-induced higher temperatures. Thus, a continuous 3D porous “multilayer” graphene supported on flexible substrates created by pulsed laser irradiation in a single pass has high production efficiency. While the exact mechanism of PI conversion into graphene is still unclear, the underlying process involves photothermal reaction. The inducted temperature with laser pulses in short exposure times provides high enough energy to let volatile species leave the monomer. Thus, the occurrence of carbonization while scribing PI surface with infrared laser is sufficient to dissociate the C–O, C=O, C–H, and C–N bonds, rearrange aromatic fragments and recombine to produce C–C bond from photothermal conversion $sp^3-(sp^3 C) \rightarrow sp^2-(sp^2 C)$ into a graphene-like aggregated structure. The rapid liberation of carbonaceous and nitric gases due to local explosions from the irradiated PI determines the observed 3D porous structure. Because of the short time scales of conversion, there exist 5-, 7- and occasional 8-membered carbon rings are occasionally present which marginally bend the ordinary 2D hexagonal lattice structure. The morphology, crystallinity, and composition of LIPG are dependent upon both the substrate and the actual laser fluence (power, speed). The use of PI precursors contains heteroatoms in their backbone (*e.g.*, nitrogen), permitted to obtain intrinsically doped LIPG and expands the rich surface chemistry and application roadmap, especially in electrochemical energy and sensing fields like for other GFNs. This laser induced single-step synthetic strategy is chemical free method for producing 3D porous graphene

in contrast to supercritical CO₂ and freeze-drying methods producing monolithic aerogels which are time consuming and require chemicals as in the case for GA and NGA also encouraging comparative study with LIPG [25]. Finally, the process of GA or NGA transfer is challenging compared with LIPG film to other soft and stretchable substrates for the fabrication of customized wearable electronics and biomedicine [101, 102].

3.2 Morphological and structural characterization

Figure 1b-1c shows the representative microscopy images of LIPG from SEM and TEM revealing surface morphology from microscale to nanoscale. They show three-dimensional multiplexed graphitic nanosheet appearing as “soap bubble” foam with microporous morphology resulting from rapid liberation of gas with occasional amorphous carbon (*a*-C). These porous structures render enhanced accessible surface area and facilitate electrolyte penetration and ion confinement into the LIPG electrode active area. Figures 1d-1e provide SEM and TEM images revealing surface morphology from microscale to nanoscale for other graphene nanomaterials: monolayer Gr, GO, CerGO, GA, NGA, and LIPG displaying from two-dimensional smooth surface to complex three-dimensional patterns, kinks and folds. The high electrical conductivity of LIPG along the trace of laser induction measured as two-terminal device prepared using conducting silver paint on two sides of regions and silver alloy wire give rise to sheet resistance ($R_s = \frac{\pi}{\ln 2} \frac{\Delta V}{I}$) ranged 20–30 Ω/cm^2 depending upon the scan speed (110–120 mm/s) and laser power (9%–12%). Corresponding electrical conductivity $\sigma (= \frac{1}{R_s \times t})$ at room temperature was around 5–7 S/cm, where t is the thickness of LIPG (≈ 40 – $50 \mu\text{m}$). As for GFNs measured in similar manner, it varied between 1 mS/cm and 5 S/cm depending upon the nanomaterials following $\text{GO} < \text{ErGO} < \text{rGO}_{\text{th}} < \text{CerGO} < \text{GA} < \text{NGA}$ trend in increasing order.

The X-ray diffractogram (XRD) in Fig. 2a from LIPG (and Fig. S2, ESI from other GFNs, rGO_{th} , ErGO, GA and NGA) show characteristics of graphene-related material along with precursor PI and GO (001) in the range $2\theta = 5^\circ$ – 60° . The major diffraction peak (002) at $2\theta = 24.8$ – 25.4° characteristic of graphene gives an interlayer spacing (I_c) of ~ 3.4 – 3.6 \AA between atomic planes, indicative of reasonably high degree of graphitization upon various processing to produce GFNs. A marginal asymmetry of (002) peak points to an increase in interplanar I_c and the expanded spacing I_c can be attributed to regions where defects are distributed on hexagonal graphene layers. Likewise, depending upon the porosity, the peaks are broadened showing

distribution of spacing attributed to surface groups. The peak at $2\theta = 42.5^\circ$ indexed to (100) reflection in LIPG is associated with in-plane lattice structure. The crystallites along the c axis (d_c) and domain size in a axis (d_a) is calculated using Eqs. (1) and (2), respectively [16, 25, 26]:

$$d_c = \frac{0.89\lambda}{\beta_{hkl}\cos\theta_{hkl}} \quad (1)$$

$$d_a = \frac{1.84\lambda}{\beta_{hkl}\cos\theta_{hkl}} \quad (2)$$

where λ ($=1.54 \text{ \AA}$) the X-ray wavelength and β_{hkl} (in radians) the full width at half maximum of (002) and (100) peaks, which are calculated to be $\sim 18 \text{ nm}$ and $\sim 34 \text{ nm}$, respectively for LIPG. As for the GFNs, the (002) peak was shifted to lower 2θ ($\sim 10\text{-}12^\circ$) for GO indicating the lattice expansion due to the presence of oxygenated functional groups and water molecules in-between the sheets unlike those for CerGO or rGO_{th} and ErGO as they represent functionalized graphene equivalents and GA and NGA for which the (002) peak appears between $24\text{-}25.6^\circ$ (Fig. S2, ESI). The Raman spectra of LIPG (Fig. 2b) and of GFNs (Fig. 2d and Fig. S2, ESI) show assignment of first- and second- order Raman spectral bands (D, G and 2D) and provide intensity ratio of D to G band (I_D/I_G) values. The spectra showed prominent Raman bands characteristic of graphitic G band at $\sim 1580 \text{ cm}^{-1}$ assigned to sp^2C stretching E_{2g} mode and disorder-induced dispersive D peak at $\sim 1350 \text{ cm}^{-1}$ corresponded to A_{1g} breathing mode of sp^2 -bonded defective graphitic phase or bent sp^2C bonds [51, 52, 53, 54]. If PI polymer would carbonize at temperatures ranging from 800°C to 1500°C , the resulting Raman spectra would resemble glassy carbon (GC) [103]. But the spectrum for LIPG and other GFNs are significantly different and representative of turbostratic structure with average sp^2C cluster or domain size determined from I_D/I_G ratio following proposed defect active model [104, 105]. The D to G band intensity ratio (I_D/I_G) indicates degree of disorder or graphitized formation in the LIPG films which is comparable to GFNs shown in Fig. 2 (and Figs. S2, ESI) except for pristine graphene (Gr) without lattice defects and surface functional groups. Using Raman spectroscopic data, the crystalline size in a axis (L_a) can be calculated following Eq. (3) [53]:

$$L_a = (2.4 \times 10^{-10}) \times \lambda_L^4 \left(\frac{I_G}{I_D} \right) \quad (3)$$

where λ_L (=514 nm) wavelength of Raman excitation. The L_a values for LIPG and for most GFNs ranged between 4–7 nm. As for defects number density, n_D (/cm²) and the inter-defect distance (L_D , nm) are calculated from I_D/I_G ratio, Eqs. (4-6) [104]:

$$L_D^2(nm^2) = \frac{(4.3 \pm 1.3) \times 10^3}{E_L^4} \left(\frac{I_D}{I_G}\right)^{-1} \quad (4)$$

and in terms of excitation laser wavelength (λ_L):

$$L_D^2(nm^2) = ((1.8 \pm 0.5) \times 10^{-9}) \lambda_L^4 \left(\frac{I_D}{I_G}\right)^{-1} \quad (5)$$

or

$$L_D(nm) = \sqrt[2]{1.26 \times 10^2 \left(\frac{I_D}{I_G}\right)^{-1}} \quad (6)$$

Subsequently, the defect number density $n_D(cm^{-2}) = 10^{14}/(\pi L_D^2)$, Eqs. (4) and (5) become:

$$n_D(cm^{-2}) = ((7.3 \pm 2.2) \times 10^9) E_L^4 \left(\frac{I_D}{I_G}\right) \quad (7)$$

or

$$n_D(cm^{-2}) = \frac{(1.8 \pm 0.5) \times 10^{22}}{\lambda_L^4} \left(\frac{I_D}{I_G}\right) \quad (8)$$

The average value of I_D/I_G used to calculate the n_D by Eq. (4a) ranged between $7.0 \times 10^{12} - 2.5 \times 10^{13}$ cm⁻² (*ca.* $0.15 \pm 0.06 \times 10^{11}$ cm⁻² for pristine graphene) for all the graphene-related materials studied [60, 83]. Next is the second-order Raman spectral D (2D) band centered at ~ 2670 cm⁻¹ originating from zone-boundary K phonons, arise due to double-resonant (DR) Raman scattering mechanism, besides combination (D+G) and second-order G (2G) bands occurring at ~ 2940 cm⁻¹ and ~ 3200 cm⁻¹, respectively for all the graphene nanomaterials investigated [51]. The Raman spectral 2D

band profile for all the GFNs can be fitted with one Lorentzian peak, analogous to monolayer graphene, but with larger full width at half maximum value $> 50 \text{ cm}^{-1}$. This band profile is typical to those in 2D graphitic structures consisting of randomly stacked graphene layers along c axis. The charge carrier or doping density (n_e) can also be determined from the average value of I_{2D}/I_G ratio [106].

The XPS (X-ray photoelectron spectroscopy) allows chemical structure via binding energies and changes in the oxidation states of the elements present on the materials surface. The high-resolution XPS spectra of the C1s region is presented in Fig. 2c for LIPG along with survey spectra and of GFNs as in Figs. S2, ESI showing how the surface contained carbon, oxygen, and nitrogen elements. The deconvolution of the main C1s peak in its components (the main peak C–C sp^2 and C–C sp^3 carbon bonds, C–O(H) epoxides and hydroxides, carbonyls C=O, and carboxyls O–C=O(H), and the π – π^* transition loss) showed low contribution from polyimide O–C=O bonds, whereas the contribution from sp^2 –C–C bonds was the highest. The N1s peak (see inset) consists of one component centered at 400.4 eV, commonly assigned to C–N bonds convoluted with a second component appearing at ~ 402.3 eV commonly assigned to oxidized nitrogen atoms. From the core level peaks of C1s, O1s, and N1s, the percentage atomic concentration of carbon, oxygen, and nitrogen was determined by dividing the peak intensities with the appropriate relative sensitivity factor after correcting them from the experimentally determined analyzer transmission characteristics. XPS spectrum shows a dominant C=C peak (285.45 eV, 47–55 *at. %*) as anticipated followed by C–C peak (284.68 eV, 8–10 *at. %*) and various oxygenated functional groups *i.e.*, C–O (286.26 eV, 28–30 *at. %*), C=O (289.26 eV, 12 *at. %*) and O–C=O (290.38 eV, 2 *at. %*) peaks along with weak C–N peak (400.7 eV, 3 *at. %*) for LIPG since the precursor PI contained nitrogen. High percentages of carbon sp^2 -type and low percentages of oxygen and nitrogen confirmed the rapid breaking and removal of C–N, C–O, and C=O and sp^2 carbon atoms occurring during the laser-induced process responsible for the formation of the porous morphology and agreeing well with other GFNs (see ref. 16 and Fig. S2, ESI). Note the N1s peak for NGA was too weak to be detectable.

3.3 Experimental electrochemical properties and determining kinetic rate constant at macroscale

This section discusses the traditional macroelectrode configuration yielding ensemble averaged electrochemical properties. A schematic illustration showing comparison between macroelectrode (planar diffusion) and microelectrode (convergent diffusion) is provided in Fig.

S3, ESI [59, 107], where the latter is discussed in the following section. Briefly, the diffusion to or from the edge of a macroelectrode (ensemble measurement) is effectively to a point (“edge effects”), therefore the current density (charge transfer rate) and mass transport (diffusion) are larger at the edge and diffusion becomes convergent (local measurement) in microelectrode configuration. During the measurement, the electrolyte was purged with argon gas using a surface bubbler to replace atmospheric oxygen. The kinetics from LIPG and GFNs electrodes in terms of cyclic voltammograms (CVs) with and without $\text{Fe}(\text{CN})_6^{3-/4-}$ redox probe are presented in Fig. 3a and Fig. 3d, respectively (see also Fig. S4 for GFNs with redox probe). The CVs present a well-defined wave shape which is usual for ET reaction under semi-infinite planar diffusion control [70]. Qualitatively, GFN electrodes are characterized with higher peak current densities with scan rates indicating that the nanosheets possess favorable micro/nanoscale porous structure possessing higher specific surface area ($\sim 900 \text{ m}^2/\text{g}$) and electronic properties effective for efficient electron transfer through the electrode/electrolyte interface. While $\text{Fe}(\text{CN})_6^{3-/4-}$ redox reaction is considered quasi-reversible with overlapping diffusion zone (*i.e.*, oxidation peak-to-reduction peak separation $\Delta E_p > 59 \text{ mV}$ in CV scan [70]), the LIPG and GFNs as active electrode materials are characterized with $\Delta E_p = 55\text{--}59 \text{ mV}$ at $\nu = 50 \text{ mV s}^{-1}$ and with $\Delta E_p = 70\text{--}80 \text{ mV}$ at $\nu = 50 \text{ mV s}^{-1}$ scan rate, respectively, meaning they show reasonably reversible behavior. Additionally, the symmetric anodic-to-cathodic current density ratio $j_a/j_c \approx 1$ gives further justification of the reversible redox process. Following the process considered reversible, a reasonable linear dependence of the $i_p = f(\nu^{1/2})$ is exhibited as in Fig. 3b indicative of diffusion-controlled ET process. Fig. 3d also shows a set of CVs for GFNs showing subtle change in their rectangular shape without the redox mediator (see also Fig. S4, ESI with redox mediator) and they were used for determining relevant parameters for a catalog of graphene-family nanoelectrodes. The values of double-layer capacitance (C_{dl}) were determined from CVs in a non-Faradaic region at different scan rates ranging between 5 and 500 mV s^{-1} and by plotting the difference current or current density $\Delta j = (j_a - j_c)$ versus scan rate, respectively. The C_{dl} was determined to shed deeper insights into improved performance and giving better knowledge about electrochemically active sites of samples. Among those studied, LIPG, NGA, and GA had a reasonable C_{dl} values of 11.2 , 10.7 , and 9.5 mF cm^{-2} compared with rGO_{th} (3.8 mF cm^{-2}), CerGO (3.5 mF cm^{-2}), GO (2.3 mF cm^{-2}) and Gr_{def} (0.62 mF cm^{-2}). The electrochemically active surface area (ECSA) was also estimated using the following relationship, $\text{ECSA} = \text{Geometrical Surface area} \times C_{dl}/C_s$, where C_s is the



specific capacitance value [38] and the geometric surface area is 0.125 cm² or 0.196 cm² [108, 109]. Since electrochemical surface area (ECSA) is proportional to C_{dl} values, the ECSA values were calculated and are tabulated in Table 1. One can also determine nominal area of the electrodes through the commonly used Randles-Sevcik equation for a quasi-reversible, one-step, one-electron reaction following [69]:

$$i_p = 2.69 \times 10^5 n \alpha^{3/2} A v^{1/2} D_0^{1/2} c_0 \quad (9)$$

where i_p is peak current (A), c_0 is the concentration of the diffusing species (mol dm⁻³), and α is transfer coefficient (0.5). The $i_p = f(v^{1/2})$ characteristics of LIPG electrode surface is plotted in Fig. 3b. From a linear relationship of $i_p = f(v^{1/2})$, the nominal active area, A ($= m / (2.69 \times 10^5 * n^{3/2} * D^{1/2} * c)$), was estimated for each electrode studied and compared with ECSA. Here m is the slope from $i_p = f(v^{1/2})$, n the number of electrons transferred ($n=1$), D the diffusion coefficient of redox probe ($= 7.3 \times 10^{-6}$ cm²/s for ferrocyanide and 6.67×10^{-6} cm²/s for ferrocene methanol), and c the concentration of redox probe (10^{-3} mol/cm³). Even if we consider our electrode surface as rough, the resulting effect on the shape of diffusion-controlled voltammograms could not be affected by a surface roughness much below 50 microns to the order of nanometers [110]. The ECSA values are greater than the nominal areas in compliance with the expectation. The specific areal capacitance (C_A , mF/cm²) based on the CV curves is determined following Eq. (10):

$$C_A = \frac{1}{2Av} \left(\frac{1}{(V_f - V_i)} \right) \int_{V_i}^{V_f} I(V) dV \quad (10)$$

where A the total geometric surface area of active electrodes (cm²); v the voltage sweep rate (V·s⁻¹); V_f and V_i are the suitable potential limits in CV curves; and $I(V)$ the voltametric current (amperes). $\int_{V_i}^{V_f} I(V) dV$ is the integrated area from CV curves. The calculated specific areal capacitance C_A for LIPG turned out to be 1.20 mF/cm² similar to GA (0.93 mF/cm²) and NGA (1.12 mF/cm²) [16, 19, 35, 53, 54, 60, 111, 112], which are manifold higher than pristine graphene (*ca.* 2-5 μF/cm²) [59]. The higher surface area graphene-family electrodes (specifically, LIPG, GA, NGA) basically tend to have electroactive chemical species, surface impurities, and defect dopant yielding relatively higher redox current density due to more accessibility for electrolyte ions. In general, the electrode surface is predominated by defective domains and thin amorphous

carbon impurity phase that provide favorable electroactive sites for effective ions transportation. The number of active sites developed through atomic scale point defects, dopant and multiplexed web of nanosheets (LIPG, GA, NGA) prevail the redox process amplified in the following sections. It is also worth noting since the surface topology can influence electrochemical performance, the ECSA-normalized electroactivity trend is different supporting the fact that the electrochemical activity is mainly due to the enhanced electrochemical surface area accounted for by limited number of exposed active sites and diffusion-controlled reaction. However, one cannot rule out the role of functional groups that indirectly contribute to achieving higher active surface area and by creating favorable environment, modifying the electronic structure thereby facilitating faster electron transfer. To validate this claim, the electrochemical impedance spectroscopy (EIS) was used to probe additional interfacial electron transfer kinetics and to determine parameters that support various interpretations.

The impedance spectra represented as Nyquist plot ($-Z''$ versus Z') plotted in Fig. 3c for LIPG (and Fig. S5 for GFNs, ESI) are fitted with an equivalent R-CPE circuit as in Fig. 3c, inset. They display semicircle pattern covering the high-frequency region, with a 45° slope line in the mid to low-frequency range attributed to subtle change in their Warburg impedance (Z_W), related to charge transfer process at the electrode-electrolyte interface and semi-infinite mass diffusion, respectively [113]. Quantitative values were extracted by fitting the data following EEQC in the EC-Lab software consisting of $R_s(CPE(R_{ct}W))$ elements (Fig. 3c, inset) [107] with normalized fitting error $\chi^2 \approx 10^{-4}$. In the proposed circuit simulation, R_s refers to the cumulative series resistance made up of electrolyte resistance caused by ions that remains same for all the electrodes, resistance inherent to the active electrode material, and interfacial resistance between the electrode and current collector, CPE (Constant phase element) represents a non-ideal behavior of electric double layer capacitance (C_{EDL} or C_{dl}) arising due to spatial heterogeneities at the electrified interfaces and hierarchical porous surface. Frequency dispersion is a commonly acknowledged behavior in the impedance response of electrode/electrolyte interfaces [9]. Generally, the frequency dispersion reflects a distribution in time constants of interfacial physicochemical processes, which has been reported to originate from surface heterogeneity of structural properties, specific anion adsorption, coupling between Faradaic and double layer charging currents, geometry-induced current and potential distributions across electrodes surface. To model this behavior, a fractional element, CPE, in impedance form is expressed as follows [114]: $Z_{CPE} =$



$1/Y_{CPE} = 1/Q(j\omega)^\alpha = 1/Q(\omega)^\alpha \exp(-j\pi\alpha/2)$, where Q is pre-exponential factor related to admittance Y , ω is angular frequency, and α is vital CPE exponent ($=1$, for an ideal capacitor, its deviation from 1 represent heterogeneity and $=0$ for a pure resistance) [115]. CPE coefficient Q , along with exponent α , are a prerequisite for the calculation of a characteristic capacitance as defined by Brug *et. al.*, [116]. Next, R_{ct} is the electron transfer resistance from electrode to the active species (or vice versa) and thus associated with redox process kinetics [115, 117]. Typically, a high R_{ct} value suggests delayed or sluggish reaction kinetics. Alternatively, smaller R_{ct} reflected in smaller semicircle indicates rapid electron transfer. From the circuit simulation fitting results, the R_{ct} values for LIPG on PI are $\sim 32.5 \Omega/\text{cm}^2$ and $5.1 \Omega/\text{cm}^2$ on ITO substrates and for GFNs, particularly for CerGO, GA, NGA electrodes, it ranged between $3.5 \Omega/\text{cm}^2$ and $6.2 \Omega/\text{cm}^2$. Furthermore, the CPE exponent α ranged between 0.83 and 0.87 for all GFNs including LIPG indicating a decrease in frequency dispersion of capacitance, increasing spatial homogeneity [19, 60, 115], and closer to a good polarizable interface. Finally, W is the Warburg impedance (Z_W) in low frequency region, and it is related to R_{ct} , diffusion coefficient, and k_{ET} by $Z_W = R_{ct}\lambda/(\omega)^{1/2}$ and $\lambda \approx k_{ET}/2\sqrt{D_0}$, where the symbols have usual meaning given electrochemical reactions are interfacial, mass transport arises due to diffusion processes. The total interfacial capacitance can be extracted from EIS data by adopting a graphical approach developed by Tribollet *et.al.*, [118] for systems exhibiting frequency dispersion effects. Effective capacitance C_{eff} is calculated at each applied frequency using the following equation: $C_{eff} = \sin\left(\frac{\alpha\pi}{2}\right) \frac{-1}{Z_{im}(2\pi f)^\alpha}$, where Z_{im} is the imaginary part of impedance, f the applied frequency in Hz. The final capacitance values were obtained by averaging the determined C_{eff} values within the frequency range where the phase angle is $\geq 75^\circ$ per absolute value. The quantitative values of the elements used for fitting the EIS data following CPE and graphical method (C_{eff}) are provided in Table 2. Summarizing the traditional electrochemical measurements, it is reasonable to conclude that surface functionality, porous and extended network of graphene nanosheets generate a reasonable faster electron transfer kinetics.

3.4 Experimental electrochemical kinetic rate measurements and mapping electroactivity using voltametric and probe approach SECM

Scanning electrochemical microscopy (SECM) has proven to be a powerful analytical technique for probing interfacial processes locally, including heterogeneous ET reaction, molecular transport across membranes, adsorption/desorption processes, corrosion processes, and

the activity of living biological cells [70, 119], with high spatial and temporal resolution. SECM is based on faradaic current changes when a tip is scanned across the sample surface, obtaining topographic and surface reaction kinetic information. Recently, it has been shown to overcome issues related to potential drop in solution (iR drop) and charging current and thus applicable to probe interfacial region. Here, we chiefly employed the application of SECM to study charge transfer at the electrode–electrolyte interface and imaging electroactivity of electrode surfaces over large area in feedback mode. Thus, it is conceivable to probe local interfacial electron transfer and determine ET kinetic rates and correlate with microscopic structure to establish *microstructure-property-activity* relationships. They are indispensable not only for understanding the electrochemical energy conversion and storage mechanisms (supercapacitive–*surface ion adsorption* and pseudocapacitive–*electron transfer*), but also for electrocatalysis, biocatalysis, and designing engineered electrodes with desired electroactivity. Hence exploring the underlying reasons behind exceptional performance by tailoring electron transfer dynamics across solid–liquid interfaces necessitated analyses by SECM technique. To employ SECM in feedback mode, the oxidized form of an appropriate OS-ET redox mediator abovementioned was used. The redox potential of the mediator was high enough to appear within the potential window *i.e.*, diffusion-controlled mediator electroreduction in a de-aerated electrolyte. Moreover, the mediator molecule was small enough to access different adsorption sites, defects, edges and micropores. Finally, it was water soluble in millimolar concentration. It is noteworthy that the ET process for potassium ferro/ferricyanide redox couple on graphene-family electrodes is largely known to be standard outer sphere reaction resulting in the reaction kinetics translating into the chemical composition and related functionality of the investigated electrode surfaces. It is because the effective electron transfer requires direct interaction with reactive sites on the electrode, which is sensitive to oxide on the electrode surface and edge hydrogen bonding sites [120]. Nevertheless, utilizing redox probes allows for effective differentiation of process kinetics that originate from a variety of active sites laying a foundational electrochemical activity roadmap for diverse graphene electrodes examined.

The cyclic voltammograms (CVs) are measured in a single compartment three–electrode electrochemical cell with SECM using disk shaped Pt tip (microelectrode configuration) highlights the unique difference between the shape of CV profiles and current magnitude as in Figs. 4a and 4b (see also Fig. S3, ESI). Alternatively, the voltammetry profiles (magnitude of current response



and peak appearance) at disk shaped microelectrode containing a supporting electrolyte and reducible redox active compound, leads to sigmoidal curves with a steady-state, diffusion-limited current, measured at electrode potentials significantly beyond the standard redox potential of the dissolved redox mediator. Figures 4a and 4b represent characteristic CVs obtained using SECM setups with ferrocene methanol redox probe at two different positions, first when the tip was far away and second when the tip is in touch with the electrolyte and nearer to the electrode surface as well as of GFNs (GO, rGO, GA and NGA). Qualitatively, the CV profiles from SECM voltametric mode reveal distinct differences in their shapes (traditional rectangular loop versus sigmoidal) with faint redox peaks corresponding to characteristic double-layer supercapacitor and the current magnitude that is an order of magnitude higher for LIPG electrode and comparable to GFNs under the electrochemical environment used. The redox reaction from aqueous hexacyanoferrate (III/II) [Ferro/Ferri cyanide] or hydroxy methyl ferrocene (I/II) probes exhibited quasi-reversible one-electron transfer behavior. It occurs across the probed electrode surface such that the ions diffusion from or to the electrode surface is described as ‘diffusion-limited’ giving rise to asymmetric CV response, also described in Fig. S3, ESI. The size, shape, and charge of the probe molecule may play *albeit* a minor role in the electrochemical reaction. Recent electrochemistry of monolayer graphene with defects (Gr_{def}) and twisted bilayer (*t*-BL) graphene electrodes elucidated heterogeneous charge transfer kinetics with the greatest enhancement superior to noble metals. These effects were driven by the mixed basal and edge plane sites that include heterogeneity disrupting sp^2 C conjugation above mentioned and the angle-dependent tuning of moiré-derived flat bands that substantially modulate electron transfer process near the magic angle [121, 122]. The synergistic effects could also result from the interaction of electrolyte ions with defects and functional groups to the extent there is heterogeneity of electronic nature (accepting or donating depending upon the functional group site).

Now, we determined heterogeneous ET rate using various approaches at macroscale (traditional) where the reaction current was recorded over the entire polarized electrode surface and microscale (via SECM) where the tip current with distance was collected locally and over smaller area discussed below. Figures 4 c and 4d provide probe approach curves plotting the normalized tip current with normalized distance as the tip approaches electrodes surface with an expected increasing tip current. The standard heterogeneous rate constant k^0 in macroscale



configuration was estimated from the CV profiles at scan rate of 10 or 20 mV s⁻¹ using the Nicholson approach following [123, 124]:

$$k^0 = \psi \cdot \sqrt{\frac{\pi D_0 \nu F n}{RT}} \quad (11)$$

where ψ the dimensionless kinetic parameter estimated from peak potential separation ΔE_p *i.e.*, $\psi = (-0.6288 + 0.0021\Delta E_p)/(1 - 0.017\Delta E_p)$, D_0 the diffusion coefficient of redox probe ((Fe(CN)₆)^{4-/3-}: 7.30×10⁻⁶ cm²s⁻¹) [Fc⁺/Fc⁰: 6.72×10⁻⁶ cm²s⁻¹], ν the scan rate (V s⁻¹), R corresponds to gas constant (8.314 J K⁻¹ mol⁻¹), F the Faraday's constant (96,485 C mol⁻¹) and T the temperature (298 °K). Likewise, the apparent electron transfer rate constant (k_{app}) was also obtained within macroscale approach following [125]:

$$k_{app} = RT/n^2 F^2 A R_{ct} c_0 \quad (12)$$

where A the experimentally determined nominal area of the electrodes, and R_{ct} the electron (or charge) transfer resistance extracted from the fitted Nyquist plot (Fig. 3c and Fig. S5, ESI) at medium frequencies discussed above. While the electron transfer process consists of several steps, the solvation / desolvation ion process has been recognized as the rate determining step for OS-ET called for a necessary reduction in activation energy to improve the reaction kinetics at the interfaces [126]. Following general (electro)chemical transition theory [127], the reaction rate

constant is given by: $k(E) = \kappa(E) e^{-\frac{\Delta G(E)}{k_B T}}$, where the potential-dependent pre-factor $\kappa(E)$ accounts for the attempt frequency in transition state theory (TST) and may include effects beyond TST such as non-adiabatic correction, and importantly solvent (aqueous) energy dynamics and $\Delta G(E)$ is the free energy barrier depending upon the electrode potential, E . More physically motivated models are based on the seminal work of Marcus [128, 129], which has been extended to include contributions not only from outer sphere component, but also adiabatic kinetics and manifold of electronic states of the electrode materials, all of which can affect the pre-factor and energy barrier discussed in the following section. Since the ion transfer kinetics is assessed by R_{ct} , a high value suggests delayed electron transfer reaction or vice versa. Thus, the defects and specific functional groups lead to reasonable redox kinetics and values of ET rate determined from macroelectrode (ensemble averaged) follow the trend: LIPG ≥ GA ≥ NGA ≥ CerGO > ErGO > rGO_{th} > Gr_{def} > Gr (see Table 3 for details). In short, for bare pristine monolayer Gr electrode, $k^0 = 1.0 \times 10^{-3}$ cm s⁻¹ is almost two orders of magnitude smaller (*ca.* 7.54×10⁻² cm s⁻¹ for LIPG and

$5.5 \times 10^{-2} \text{ cm s}^{-1}$ for NGA). Assuming that only variable is R_{ct} , the estimated k^0 for *a*-C (amorphous carbon) and CNW (carbon nanowalls) were $1.3 \times 10^{-3} \text{ cm s}^{-1}$ and $0.9 \times 10^{-2} \text{ cm s}^{-1}$, respectively [130, 131]. It is also worth noting that for variants of graphene nanoelectrodes prepared from thermal reduction of precursor GO (rGO_{th}) was ineffective as compared with chemical (CerGO) and electrochemical reduction (ErGO) with higher conductivity for scalable and practical use. The introduction of defects, functional groups and N dopants into the graphene sheets, predominantly determined through Raman spectra and XPS analysis, played a significantly important role in the observed ET values. Furthermore, the formation of sp^2 hybridized carbon (sp^2 C) phases enriched with edge dislocation, hydrogen bonding sites and large electrochemical surface area, apparently contribute to the improved electrochemical rate making these electrodes persistently attractive. It is also important to note that the electron and mass transport (diffusion) at the electrified interfaces may result in modifications that can markedly influence the electron density and subsequent reaction pathways. From a macroscale approach, it can be concluded that the presence of defects density is crucial to facilitate enhanced ET rate constant useful for modern applied electrochemistry.

Next, we move to microelectrode configuration to determine local heterogeneous ET rate, k_{ET} , by detecting redox reactions occurring proximity to electrode surface. SECM is used to obtain quantitative information of local reaction rates where an ultramicroelectrode tip is moved from bulk solution toward the surface (substrate) under study and the tip current (i_T) is measured with respect to *z*-distance to obtain “probe approach curves” [60] in feedback mode. The tip is held at $V_t = 0.4 \text{ V}$ to ensure the redox species in solution is oxidized such that diffusion-limited current (sub-nanoampere sensitivity) is obtained. The potential of graphene electrodes was kept at around 0.1 V (equivalent to OCP, *i.e.*, within Faradaic window) to reduce redox probe species generated at the tip. A diffusion controlled steady-state tip current far from electrode surface ($i_{T,\infty}$) of redox probe electroreduction follows: $i_{T,\infty} = 4nFCDr_{tip}$, where *n* the number of electrons transferred at the electrode tip ($O + ne^- \rightleftharpoons R$), *F* Faraday constant, *C* concentration of oxidized redox probe species and *D* the diffusion coefficient limited by hemispherical region (local *D*). Figures 4c-4d show probe approach curves for LIPG and GFNs (GO, CerGO, ErGO, GA, and NGA) at different electrode-tip distances showing normalized tip current ($i_T/i_{T,\infty}$) behavior with normalized distance, $L = d/a = 1$, where *d* the electrode-tip distance (same as *z*) and *a*, the tip radius (same as r_{tip}). Qualitatively, as tips approach the surface of heterogeneous conductive surface, the reduced



species formed at the tip is oxidized yielding an increased tip current observed. The nonlinearity in approach curves is apparent and the extent of positive feedback experienced by the tip depends upon the reaction rate between the redox mediator and electrode surface. The procedure describes the measurement and fitting of the normalized tip current following diffusion-controlled kinetics theory at the microelectrode with analytical approximation of Cornut and Lefrou fit for $RG = 10$ (or 25), and $r_{\text{tip}} = 10 \mu\text{m}$ is provided (see section S5 and Fig. S6, ESI) [132]. The first-order normalized ET rate constant $k' = \kappa/k_{\text{eff}}$ (k_{eff} same as k^0 or k_{ET}) values are quantified for each of the graphene electrodes [33, 60]. For pristine graphene (Gr) it is found to have $k^0 = 1.1 \times 10^{-3} \text{ cm/s}$ and this value is lower than reported values from 2×10^{-2} to $4.2 \times 10^{-2} \text{ cm/s}$ for pristine CVD graphene in aqueous media [44, 107, 133]. The difference is due to the intrinsic quality of exfoliated graphene studied and CVD grown graphene, the latter tended to have atomic level defects. As for the κ values, it varied between 0.02 to 1.8 for all the electrodes from pristine to defective graphene-Gr_{def}, GO, CerGO, rGO_{th}, ErGO, GA, NGA, and LIPG and the corresponding local k_{ET} value ranged between $1.1 \times 10^{-2} \text{ cm/s}$ and $6.8 \times 10^{-1} \text{ cm/s}$, which shows twenty fold higher pointing at more electroactivity with moderate increase in defects in the basal plane and abundant edge plane sites especially in GA, NGA and LIPG electrodes. We also used empirical nonlinear approach to fit probe approach curves yielding first-order ET rate constant, k_1 (equivalent κ in Cornut and Lefrou fit) [section S5, ESI]. In general, depending upon the feedback (conductive electrode creating regenerative “positive” feedback versus insulating electrode surface prohibiting the regeneration a “negative” feedback), it follows Eqs. (13) and (14):

$$i_T^c(L) = \frac{i_T}{i_{T,\infty}} = [k_1 + k_2/L + k_3 \exp(k_4/L)], i_T > i_{T,\infty} \quad (13)$$

and

$$i_T^{\text{ins}}(L) = \frac{i_T}{i_{T,\infty}} = 1/[k_1 + k_2/L + k_3 \exp(k_4/L)], i_T < i_{T,\infty} \quad (14)$$

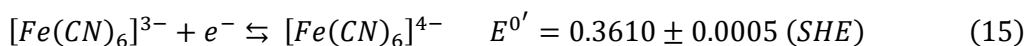
where k_1 , is first-order (single electron) and k_2 is higher order (multielectron) rate coefficient as well as k_3 and k_4 which are fitting parameters describing more complex convoluted processes related to electron transfer and mass transport that depend on the RG value and normalized distance

$L = d_0 - d_{\text{exp}}/a$ is determined by fitting the curves. The steady-state tip current can determine diffusion coefficient of redox species for all the graphene materials investigated that ranged between $6.3 \times 10^{-5} \text{ cm}^2/\text{s}$ – $2.5 \times 10^{-7} \text{ cm}^2/\text{s}$ and follow: $\text{Gr} < \text{Gr}_{\text{def}} < \text{GO} < \text{rGO}_{\text{th}} < \text{CerGO} \leq \text{ErGO} < \text{GA} < \text{NGA} \leq \text{LIPG}$ order complying with traditional macroscale approaches. They are determined by fitting d_0 in L and RG for all the heterogeneous kinetics at the tip and diffusion-controlled mediator regeneration at the substrate samples. The feedback approach curve then represents a measure for the absolute distance and the k_{ET} the effective rate from localized regions. Table 3 summarizes results from both the approaches (macroelectrode and microelectrode) and lists the k_{ET} values with accuracy of $< 1\%$, which are usually smaller than typical experimental uncertainties. It is interesting to note that for GA, NGA, and LIPG, $[\text{Fe}(\text{CN})_6]^{4-/3-}$ redox couple may exhibit limited inner-sphere electron transfer kinetics, with heterogeneous electron transfer rate constants values that remain notable among carbon-based electrodes. The interfaces of these three-dimensional morphologies demonstrate unique electrochemical properties, where outer-sphere mechanisms preserve redox probe structure during electron transfer, enhanced by intrinsic electrical conductivity and surface characteristics [134]. Moreover, Muzyka and Wu [76] investigations demonstrated enhanced current responses for various redox species on GFNs compared to conventional carbon electrodes, attributable to porous architecture and reactive edge site abundance suggesting underestimation of topology and wettability factors. Subsequent analyses revealed nonlinear correlations between peak potential separation and k_{ET} , suggesting potential underestimation of topology and wettability factors by the Nicholson method. This observation indicates that nano and microscale porous electrode layers modify mass transport regimes, introducing thin-layer contributions associated with analyte penetration into porous structures. Moreover, optimal oxygen functionalities enhance laser-scribed graphene (LSG) wettability, particularly benefiting $[\text{Fe}(\text{CN})_6]^{4-}$ redox mediator interactions, with minimal variations in peak separation values revealing unique behavior of 3D graphitic carbon, contrasting with previous observations of surface passivation by inner-sphere redox mediators [63].

The visualization of electroactivity is probed in constant height imaging mode taking advantage of an amperometric tip current that originates from the redox mediator, which can be modulated by variation in the tip-to-sample distance. Keeping the tip height fixed (equivalent constant current mode), the position of the tip is scanned in the xy plane to obtain multiple plots of the feedback current generating electroactive patterns from electrode regions locally. In the case



of feedback imaging presented here, the redox reaction proceeds only directly over the microelectrode where the generated redox ions/electrons are available. Thus, the SECM feedback images result from the Faradaic reaction:



Moreover, the imaging resolution of SECM depends strongly on the tip microelectrode size and the tip-substrate distance. The experimental results revealed that the highest imaging resolution was obtained with the smallest tip electrode when $d/a = 1$, and when the size of the tip electrode is fixed (10 μm), and the smallest tip-substrate distance. Figures 5 display SECM images in $500 \times 500 \mu\text{m}^2$ or $600 \times 600 \mu\text{m}^2$ area scans as two- dimension contour and three-dimension ‘heat maps’ generated using Origin software, for Gr_{def} , GO, CerGO, rGO_{th} , GA, NGA, and LIPG, of which surface morphology is shown in Fig. 1. Qualitatively, the normalized feedback current distribution correlates with electrodes structure above the defective and edge sites regions that are different from each other indicating that the electrochemical activity depends largely upon lattice imperfections and defect structure. Typically, the electrode surfaces evidenced some reactivity featured through the broad hills and valleys and highly localized electroactive sites, also called “hot spots”. Generally, the peaking values were comparable among GFNs, demonstrating that the electrochemical reactivity was improved as compared with pristine graphene monolayer (Gr). Higher overall reduction currents and higher contrast especially in Gr_{def} , CerGO, GA, NGA, and LIPG confirm the heterogeneous distribution of kinetic ET rate constant and electroactivity. On the other hand, homogeneously active surface variations in the tip current reflect the mapping of topography as opposed to local electroactivity. Quantitatively, the samples yielded several regions of highly electroactive sites with areal site density distribution of $\sim 20\text{--}70 \mu\text{m}$ along x and y regions corroborated with surface morphology of the areas probed.

The other perspective to consider on SECM imaging is to point out that the graphene nanosheets of the investigated electrodes are either randomly distributed (Gr, Gr_{def} , GO, CerGO, ErGO, rGO_{th}) and/or vertically configured (GA, NGA, LIPG) with proximity to one another within 500 nm such that they are spatially and electrochemically heterogeneous presenting regular cavities whose spatial zones display “contrasting” electrochemical behavior toward the same redox probe. Therefore, electrode surfaces/interfaces may be associated with “diffusion domain” concept



[135] such that the carbon vacancies, functional groups and N doping sites affect the heavily overlapping diffusion zones. To reinforce this assumption, the electrode surface configurations must be associated to the size of the diffusion zones. From CVs displayed in Figs. 3a and 3d (and Fig. S4, ESI), the size of the diffusion layer (δ) can be estimated using Einstein's equation $\delta = \sqrt{2Dt}$, where D the diffusion coefficient and t time. Equivalently, considering the potential width ΔE of the voltammograms for a given scan rate v , the diffusion layer width is: $\delta = \sqrt{2D \left(\frac{\Delta E}{v} \right)}$. Using appropriate potential width, $\Delta E = 0.4$ V, $v = 50$ mV/s, and $\text{Fe}(\text{CN})_6^{3-/4-}$ as redox probe with $D = 7.3 \times 10^{-6}$ cm²/s, the size of the average diffusion layer width in each isolated vertical graphene nanosheet is about 80 microns. Thus, we infer that since the spacing between the nanosheets is much smaller ($\approx 1\text{--}20$ nm) than the calculated diffusion layer width suggestive of the adjacent individual diffusion zones interact and are overlapping thereby increasing the electrode-electrolyte interfacial area summarized in Table 1. This behavior also depletes the ions and spaces between the nanosheet neighbors and significantly increases the contribution of planar diffusion indicative of the degree of adiabaticity.

The SECM imaging visually confirms the successful distribution of electroactive sites over localized areas which are generally in accordance with the Raman spectral D band arising due to lattice imperfections. Therefore, it is instructive to correlate k_{ET} values (via SECM) to defects number density n_{D} (via Raman spectroscopy). A quantitative formula was proposed to correlate the inter-defect distance, L_{D} with the intensity ratio $I_{\text{D}}/I_{\text{G}}$ as in Eqs. (3) and (4). In case of low defect density, the defects are independent, and the graphene (Gr) is partially activated with increasing defect density, the monolayer graphene (Gr) and related nanomaterials (GFNs) becomes fully activated when $L_{\text{D}} > 3$ nm *i.e.* outside the activated area [35, 60, 104, 105, 136]. Indeed, we observe an enhanced k_{ET} values 1.11×10^{-2} cm s⁻¹ to 3.8×10^{-2} – 5.5×10^{-2} cm s⁻¹, 5.6×10^{-2} – 10.01×10^{-2} cm s⁻¹, 3.2×10^{-1} cm s⁻¹, and 6.5×10^{-1} – 6.79×10^{-1} cm s⁻¹ for pristine (Gr), defective graphene (Gr_{def}), graphene oxide variants (GO, CerGO, rGO_{th}, ErGO), aerogels (GA, NGA), and LIPG with defect density ranging from 1.0×10^{11} cm⁻² to 6.0×10^{11} cm⁻², 1.5×10^{12} cm⁻² and 2.2×10^{12} cm⁻², corresponding to L_{D} from 48 to 8 and 3 nm as an upper bound, respectively. Note that the highest defect density determined in this study (2×10^{12} cm⁻²) is lower than that of fully disordered graphene (*ca.* 10^{15} cm⁻², one defect per four carbon atoms) [136]. The results following the SECM and micro-Raman spectroscopy help to establish *quantitative structure-property-electroactivity*



relationships. Data plotted in Fig. 6, panel a, suggests correlation trends between kinetic rate constant k_{ET} and atomic scale defects density n_D (or L_D) along with a detailed illustration (Fig. 6, panel b) summarizing the versatility of chemical composition, morphological diversity, lattice imperfections and specific defects in graphene-family nanomaterial electrodes. By balancing defect density while maintaining structural integrity and retaining much of the electronic conductivity, the optimal k_{ET} via SECM was attained over the smaller scanned areas (approximately $30 \times 50 \mu m^2$). As for structural defects characterized by XPS as in Fig. 2c (and Fig. S2, ESI), it shows primarily sp^2C along with oxygen moieties chiefly associated with hydroxyl ($-OH$) and carbonyl ($C=O$) groups with a small percentage carboxyl ($-COOH$) groups and sp^3C ($C-C$) bonding. The hydroxyl groups are thermodynamically stable and in fact they are incorporated at vacancy sites and may help to stabilize the defect by bonding to the under-coordinated carbon atoms. The presence of $C-N$ bonds in NGA (likely also in LIPG) besides defects and $C-O$ bonds possess differing and tunable electrochemical (re)activity depending upon the location and hybridization, showing acid-base chemical properties such as electron withdrawing effects of sp -hybridized oxygen (carbonyl groups) and electron donating effects of sp^2 -hybridized oxygen (hydroxyl and carboxylic groups). Moreover, it is reported that the negatively charged pyrrolic-N and pyridinic-N and the positive charge on quaternary-N and pyridinic-N-oxide help in electron transfer through interfacial interactions [35, 137, 138]. The oxygen groups tend to attach with defects easily and nitrogen atoms contribute to increased surface area as they are located at the periphery of graphene and carbon nanowall edge planes [60, 139, 140, 141]. Our results also highlight morphology, mostly considered and modelled as flat as an important parameter to enable efficient proton transport besides curvature (introduced through Stone-Wales pair and octagons as in LIPG) that can be an additional degree of freedom contributing toward higher or lower tip current depending upon n - (+ve curvature) or p - (-ve curvature) type semiconductive behavior [142]. It has long been debated whether these networks contain positive curvature, as seen in fullerenes, or negative curvature proposed for the Schwarzite structures, or zero curvature, as in flat graphene sheet [52, 53]. Although all three topological elements maybe present, negatively curved structures present in LIPG reporting the presence of a few octagons [52, 54] in contrast to positive curvature in other GFNs. At an atomic level, analysis of local environment shows that sp - and sp^3 - C bonded atoms are associated with line defects



and screw dislocations that resolve topological complexities such as termination of free edges and stacking of low curvature regions [53]. All these findings suggest that a moderate defect density referred as mono-/divacancies, local topological defects (Stone Wales or pentagon-heptagon (5–7) pair within hexagon), and edge plane sites, at which the tip current tended to peak which is necessary for good electroactivity. Surface functionalities associated with π bonding and robust interconnected topological conductive network are exciting for optimal electrochemical performance, especially for electrocatalytic reactions where defects act as source for active sites for ion adsorption and redox reaction, not electrochemical sink.

3.5 Density Functional Theory predictions of the electronic structure of pristine and defective graphene electrodes correlated with ET rates

Here in these sections we combine insights gained from constant potential DFT with the electrochemical rate theory to understand the nature of the ET and how it changes with graphene-family electrodes microstructure. The physical interpretation of quantitative standard ET rate (k^0 or k_{ET}) not only agrees with the theory but also cannot be interpreted in isolation thereby requiring consideration of factors including redox mechanism, defects, local density of states surrounding defect/imperfections near Fermi level, electric double-layer and quantum capacitance discussed below.

Semi-classical Gerischer-Marcus Model. Combining experimental investigations with physical model and DFT calculations further our insights into the relationship of k_{ET} with various aspects of graphene-related electrodes. The ET kinetics on pristine and defective graphene is carried out by applying Gerischer–Marcus model [68]. Accordingly, the energy distribution function of the oxidized, W_O and reduced, W_R states of a redox couple are described by Gaussian distribution with mean at $E_{F, redox} + \lambda$ and $E_{F, redox} - \lambda$, respectively and a standard deviation of $\sqrt{2\lambda k_B T}$ [143, 144, 145]:

$$W_O(\lambda, E) = \frac{1}{\sqrt{4\pi\lambda k_B T}} \exp \left\{ -\frac{(E - E_{F, redox} + \lambda)^2}{4\lambda k_B T} \right\} \quad (16)$$

$$W_R(\lambda, E) = \frac{1}{\sqrt{4\pi\lambda k_B T}} \exp \left\{ -\frac{(E - E_{F, redox} - \lambda)^2}{4\lambda k_B T} \right\} \quad (17)$$

where λ the reorganization of energy and $E_{F, \text{redox}}$ the electrochemical potential of electrons in solution. The heterogeneous ET is possible between states with the same energy and therefore, the oxidation rate constant is proportional to product of density of occupied electronic states, $W_R(\lambda, E)$ and the density of unoccupied states of the graphene electrode $(1 - f(E - E_F + |e|\eta))\rho_G(E)$ in solution. Corresponding k_{ET} between graphene(s) and $K_3Fe(CN)_6$ (or $FcMeOH$) redox probe is described for oxidation, k_O and for reduction, k_R rate constant:

$$\begin{aligned} k_O &= \frac{2\pi|H(d)|^2}{\hbar} \Delta z \int_{-\infty}^{\infty} W_R(E)(1 - f(E - E_F + |e|\eta))\rho_G(E, \eta) dE \\ &= \frac{2\pi|H(d)|^2}{\hbar\sqrt{4\pi\lambda k_B T}} \Delta z \int_{-\infty}^{\infty} \exp\left\{-\frac{(E - E_{F, \text{redox}} + \lambda)^2}{4\lambda k_B T}\right\} (1 - f(E - E_F + |e|\eta))\rho_G(E, \eta) dE \\ &= \frac{2\pi|H(d)|^2}{\hbar\sqrt{4\pi\lambda k_B T}} \Delta z \cdot k'_O(\rho_G, \lambda, \eta) \end{aligned} \quad (18)$$

and

$$\begin{aligned} k_R &= \frac{2\pi|H(d)|^2}{\hbar} \Delta z \int_{-\infty}^{\infty} W_{ox}(E)(f(E - E_F + |e|\eta))\rho_G(E, \eta) dE \\ &= \frac{2\pi|H(d)|^2}{\hbar\sqrt{4\pi\lambda k_B T}} \Delta z \int_{-\infty}^{\infty} \exp\left\{-\frac{(E - E_{F, \text{redox}} - \lambda)^2}{4\lambda k_B T}\right\} (f(E - E_F + |e|\eta))\rho_G(E, \eta) dE \\ &= \frac{2\pi|H(d)|^2}{\hbar\sqrt{4\pi\lambda k_B T}} \Delta z \cdot k'_R(\rho_G, \lambda, \eta) \end{aligned} \quad (19)$$

where $f(E)$ the Fermi-Dirac distribution function, ρ_G the electronic density of states (DOS_G) of graphene, $W_O(\lambda, E)$ the probability density function of the oxidized (unoccupied) states, and E_F the Fermi energy of the electrode. k'_O (k'_R) are dimensionless integrals (equivalent of experimental κ in Cornut and Lefrou fit) for ET kinetics. Note that this model contains simplification in which the structure of reaction in solution is omitted while still containing the distance (d) dependence of the coupling element $H(d)$ through which one can assess the degree of adiabaticity of the OS-ET. Within this quantitative physical model, the ion-pair affects both the pre-factor, and the energy barrier mentioned above. The former is constant for a given redox couple-electrolyte system and modifies the reaction barrier through electrostatic interactions. Also, to mention, the distance between $[Fe(CN)_6]^{4-/3-}$ and the electrode support for graphene differs by about a solvated layer of 3\AA , while larger for defective graphene, GO, CerGO, rGO_{th}, and more for GA, NGA and LIPG electrodes yielding significant adiabatic contribution affecting ET kinetics. Thus, it will be reflected in the distance-dependent coupling constant, $H(d)$, entering the pre-exponential factor in



rate theory as: $\kappa_{nonadiabatic} = \frac{2\pi}{h} \frac{H(d)^2}{\sqrt{4k_B T \lambda}}$ in contrast to adiabatic ($\kappa_{adiabatic} \approx \frac{k_B T}{h}$) only contribution [128].

Nevertheless, it is challenging to quantify the adiabatic versus nonadiabatic contributions experimentally.

Given the unusually high sensitivity of k^0 (or k_{ET}) for the redox probes employed, they are useful indicators to probe graphene electrodes surface. ET kinetics is determined by integrating electronic states (number electrons) for solid electrodes and number of oxidized states of redox probe near the Fermi level for a reduction reaction [68, 146]. Subsequently, MD (Molecular Dynamics) simulation showed that the distribution of redox-active components substantially depends on the electrode material, their morphology, solvent type, surface electronic properties, electrode potential and quantum capacitance [147]. It is pertinent to elucidate that k_{ET} improvement can be understood by finite electronic DOS in the vicinity of Fermi level (E_F). Figures 7a-7b show the computed DOS of pristine (Gr), defective graphene (Gr_{def}) with mono-/di-/quad- vacancies, functionalized graphene with ($-COOH$; GO, $-OH$; rGO, N substituted; N-rGO, and NGA) groups along with optimized geometric structures as periodic cell (left panels), which are modeled as monolayer slab of 6×6 hexagonal periodic lattice. Also provided are the DOS spectra of hydrated graphene with and without defects as in Fig. 7a. It turns out that for optimized structures, there is an out of plane displacement of atoms giving rise to buckled wavelike 3D structures [148]. In short, the pristine Gr unit cell contains 72 carbons with lattice parameters $a = b = 14.15 \text{ \AA}$, Gr_{def} contains vacancies as ghost atoms, GO contains same number of epoxide (C–O–C) and hydroxyl (OH) groups and N-doped graphene configuration: pyridinic N-doped graphene (3N and 4N). Carboxyl ($-COOH$) and carbonyl ($-C=O$) groups appearing at the graphene edges are considered for NGA. Note that the 3N- and 4N-pyridinic defects have one and two carbon vacancies, respectively. The DOS of the pristine graphene is insufficient near E_F , which hampers good electrochemical activity. With the introduction of mono and divacancies, topological point defects, heteroatoms (substitutional N doping), and functional groups it modifies the electronic structure significantly by inducing mid gap states near the Dirac point (or Fermi level proximity) localized at the defect that enlarge overlap between electronic states of GFNs and redox probe molecule, which facilitated an improved ET rate from graphene to redox probe molecule [149]. Notice also that DOS is insufficient near the Fermi energy (E_F) for NGA when substituted N is adjacent to another N. While the electrons are equally distributed between all carbon atoms, the point defects



(Fig. 7a for mono-, di-, and multi- vacancies) and functional groups (Fig. 7b for oxygenated and N substituted graphene) change this uniform distribution discreetly so there are localized defect states with a narrow peak in the density of states near E_F . Additionally, for NGA where N is a substituted donor impurity, it leads to Fermi level shift from 0.41 eV to 0.94 eV energies depending upon the type of N functional group in combination with oxygenated group. The electronic states for defective graphene are found to be located directly at the defect sites. This mechanism is consistent with the proposition that the low DOS surface exhibits slow ET kinetics to OS-ET redox systems and that defects increase the DOS near the Fermi level proceeding possibly in quasi-adiabatic regime. Thus, the electroactivity must be near the defect site or defect activated region (~3–5 nm) determined from Raman spectroscopy.

3.6 Effects of quantum and double-layer capacitance and standard redox potential on the ET rate constant

Recent experimental and theoretical results indicated that the total interfacial capacitance of low-dimensional carbon electrodes, such as CNTs (having van Hove singularities, vHs) and graphene (with Dirac nodes), is associated with the relative contributions of differential electrochemical double-layer or Helmholtz capacitance (C_{EDL}), Gouy-Chapman (or diffuse) layer (C_{GC}), and the space charge or quantum capacitance (C_Q), the latter often overlooked in the reports while discussing the supercapacitors and determined from complex theoretical calculations. Typically, for electrolyte concentration above 0.1M, C_{GC} becomes larger, and its contribution decreases with electrolyte concentration. Moreover, it is known that due to extremely low density of states near Fermi level at Dirac nodes, pristine graphene (Gr) exhibits low quantum capacitance (C_Q) compared with C_{EDL} and therefore it limited the supercapacitors' energy storage capacity at low applied potential [150, 151, 152]. Thus, the total interfacial capacitance (C_{Total}) governed by cumulative effect of C_Q and C_{EDL} is represented as two capacitances connected in series as in Fig. 8a, expressed as: $1/C_{Total} = 1/C_{EDL} + 1/C_Q$. Figs. 8b-8f summarize the grand scheme of energy band alignment for graphene-based electrode and redox probe containing electrolyte and Fig. 8g shows schematic of the EDL capacitance of pristine, defective and N-doped graphene within the operating potential window. For example, Fig. 8b and Fig. 8c show DOS_G in uncharged or non-electrified defect-free graphene and energy distribution in molecular redox species in solution where the peak represents the oxidized (*unoccupied*) $W_O(\lambda, E)$ and reduced (*occupied*) state $W_R(\lambda, E)$. The Fermi level of graphene (*i.e.*, Dirac point, horizontal dashed line) shifts relative to its

vacuum level ($E'_F - E_{vac} = E_F^{vac} = -W = 4.6 \text{ eV}$ = work function) upon contact with electrolyte ($E_{F,redox}$) since they are not equal. Fig. 8d shows energy alignment during equilibration in classical limit ($C_Q \gg C_{EDL}$) in which DOS_G shifts by ΔE_{EDL} as a whole and in quantum limit ($C_Q \ll C_{EDL}$) the Fermi level shifts by ΔE_Q to $E_{F,redox}$ as in Fig. 8e [153, 154]. It is likely that during voltammetry experiments, cumulative shifts occur seen in Fig. 8f as a mixed case affecting the electrode kinetics such that:

$$E_{F,redox} - E_F^{vac} = \Delta E_{EDL} + \Delta E_Q \quad (20)$$

Consequently, graphene of different chemical structures and morphologies yield different rate constants determined experimentally due to morphological structure promoted variations in the DOS_G corroborated with theoretical calculations conducted briefly afore mentioned.

Quantum capacitance is defined by $C_Q = \frac{d\sigma}{dV}$, where $d\sigma$ is the differential surface charge density and V is the local potential. The displacement of the Dirac points by ΔE_{EDL} determined by the electric potential drop $\frac{\Delta E_{EDL}}{|e|}$ across the double layer is estimated from:

$$\sigma = -\frac{C_{EDL}\Delta E_{EDL}}{|e|} = \frac{|e|}{A} \int \rho_G(E - \Delta E_{EDL}) \times [f(E - E_F^{vac} - \Delta E_{EDL} - \Delta E_Q)] dE \quad (21)$$

where A graphene surface area. C_{EDL} is assumed to be constant and equal to an optimal value of $2\text{--}5 \text{ } \mu\text{F}/\text{cm}^2$ for pristine graphene [60, 150]. If an overpotential η is applied, Eq. (20) takes the form: $E_{F,redox} - E_F^{vac} - |e|\eta = \Delta E_{EDL} + \Delta E_Q$. Fig. S7 and section S6 (ESI) plots the effect of overpotential on ET kinetic rate constant and it is apparent that the integrated area of integrands at positive overpotential $\eta = +0.2V$ is larger than that at negative overpotential $\eta = -0.2V$. Therefore, it leads to asymmetrical dependence of the rate constant $k'_R(\eta) + k'_R(\eta)$ relative to the point $\eta = 0$. The theoretical work demonstrates that the defects and dopants affect the C_{EDL} by tuning C_Q , which originates from the change of the graphene band structure [103, 118] what has been discussed here and elucidated experimentally.

To reiterate, introducing topological point defects and dopants, complex web of graphene nanosheets comprising three-dimensional network with edges and chemical functional sites improve the electrochemical performance by maximizing the specific (areal and gravimetric) capacitance. In addition to defect sites (Gr_{def} , rGO_{th} , CerGO), the porous form of graphene (GA,

NGA, LIPG) possesses higher specific surface area, SSA (*ca.* $\sim 1,000\text{--}1,200\text{ m}^2\cdot\text{g}^{-1}$), thereby augmenting the interfacial contact area and interaction between electrolyte and electrode with weak nonadiabatic limit. The EDL capacitance (C_{EDL}) of graphene-based electrodes with different concentrations of lattice imperfections were analyzed by electrochemical impedance spectroscopy (EIS) with maximum value of $>1.1\text{ mF}/\text{cm}^2$ (*ca.* $C_{\text{EDL}} = 5\text{ }\mu\text{F}/\text{cm}^2$) having the same origin as described in previous section and literature. Our work provided a comprehensive understanding of the correlation between the atomic-scale structures and the C_{EDL} and presented a strategy for the development of theoretical models discussed. Since C_{EDL} determines Dirac point shift (ΔE_{EDL}) when two phases are in contact, the electrochemical response is tunable by varying C_{EDL} . For classical limit ($C_{\text{Q}} \gg C_{\text{EDL}}$) the electrode band structure is same with respect to $E_{\text{F, redox}}$ and k^0 is independent of standard potential V^0 . Consequently, the higher value of k'_0 is proportional to DOS near $E_{\text{F}}^{\text{vac}}$. Also, with increase in C_{EDL} as observed here, the quantum capacitance begins to make contribution towards k'_0 (Fig. 8h). The enhancement of the quantum capacitance can be ascribed to the formation of localized states near Dirac point and/or shift of Fermi level induced by the defects and doping such there is an optimal wavefunction overlap. Therefore, the observed current is mainly due to the charging/discharging of EDL at graphene/electrolyte interface. The following work has backed up the findings seen in Fig. 8h that plots variation of k'_0 for pristine (Gr) and defective graphene (Gr_{def}) with C_{EDL} in classical and quantum limits ($\sim 2\text{--}20\text{ }\mu\text{F}/\text{cm}^2$) [38]. Fig. 8i shows the influence of deliberately introduced defect electronic structure on dimensionless standard electron transfer rate between graphene and redox couple overpotential (*i.e.*, $k'_0 = k'_{\text{O}(\eta=0)} = k'_{\text{R}(\eta=0)}$). The standard redox potential V^0 *versus* SHE (Standard Hydrogen Electrode) is depicted by vertical lines for OS-ET in Fig. 8 [155]. At $V^0 = -0.2\text{ V}$, when $\Delta E_{\text{EDL}} = \Delta E_{\text{Q}} = 0$, the main contribution to ET is through levels lying near the Dirac point which is lower and hence k' is lower. The solid curve represents the standard rate constant for pristine Gr sample. The ET value increased by order of magnitude at V^0 from -0.2 to $+0.2\text{ V}$, demonstrating the strongest ET acceleration due to sharp peak in DOS near the Fermi level (see Fig. S7, ESI). Several experiments included in this study where an increase in the rate constant by at least an order of magnitude or >50 -fold increase is found as compared to traditional monolayer graphene. It is ascertained that defects, dopants, and edges sites are pivotal for improved local electroactivity for graphene-family nanoelectrodes for future electrochemical technologies. Experimental analysis together with theoretical/computational became significant to reveal the variations in electrochemical activity



by edge sites density, doping and ‘topological defects’ where flat bands are localized and produce a large local electrochemical enhancement that cannot be accounted for by the presence of local density of states alone.

4. Conclusions

In summary, we examined the interplay of lattice imperfections such as topological point defects, mixed basal and edge plane sites, N dopant, morphological diversity, and electrochemical surface area on the adiabatic electron transfer (ET) kinetic rates (k^0 or k_{ET}) across graphene-family nanomaterial electrodes as well as electroactivity imaging, serving as a benchmark for a fair assessment of emerging electrodes. The results exhibited synergistic effects of enhanced ET by almost fifty-fold faster than that of pristine monolayer graphene due to electronic band-engineering exemplified by the presence of density of states due to favorable defects in the vicinity of Fermi Level. They in turn influence the quantum capacitance that is connected in series with Helmholtz capacitance and modify the total interfacial or electric double-layer capacitance (C_{EDL}). Fundamentally, due to small quantum capacitance, the electron transfer and ion transportation are tunable by the variation of C_{EDL} from redox-independent behavior to the DOS-like dependence of the standard rate constant. To rationalize our findings, we showed that a combined experiment-theory-modeling constitutes a powerful tool to elucidate the mechanistic details that govern ET kinetics toward elementary electrochemical redox reaction within the adiabatic regime and helped to establish quantitative *microstructure-property-electroactivity* relationships. Specifically, the discrepancy in the reported k^0 values under the same conditions arises due to the sample electrode variation, particularly when the electronic disturbance is significantly larger than the local defect itself. It was also possible to rank defects according to their electrochemical activity as carried out in this work. The availability of carboxyl groups, N doping and hydrogen bonding sites on edge planes have different polarizability and local dipoles than the perfect basal plane in pristine graphene leading to spatially heterogeneity. Our extensive investigation showed the strength of complementary theoretical, physical model and experimental analysis in modern electrochemistry in designing better electrochemical energy and sensing systems for a large body of applications utilizing nano-functionalized electrode materials. We elucidated the ET kinetics tunability underlines the significance of optimized graphene-based electrodes leading to wide ranging electrochemical implications at the grand challenges of clean *energy-water-sensing nexus*, where precise control of electron transfer is indispensable (e.g., selective electrocatalysis and

electrochemical transduction).

Our results opened many opportunities to explore the impact on systems involving different electrolytes by taking advantage of in-situ capability supported with reactive force DFT and molecular dynamics calculations. As a future prospect, scanning electrochemical cell microscopy (SECCM) that combines reagent delivery from the nanopipette with electron transfer at the conductive substrate and ion transfer across the liquid/liquid interface supported at the nanopipette tip will be useful [156]. This approach offers potential advantages for measurements of ET kinetics by enabling straightforward separation from the contributions of surface topography and reactivity features to the tip current besides mapping. Lastly, pertinent to mention that our experimental findings and interpretations claim that electrochemistry and nanoscale electronics within the quantum mechanical interpretation of joint electron / ion dynamics have a common foundation in quantum physics and quantum chemistry useful for modern nanoscale electronic and electrochemical devices.

Acknowledgements

The corresponding author (S.G.) acknowledges financial support for these studies from Gdansk University of Technology by the DEC-37/2022/IDUB/1.1/NOBELIUM grant under IDUB Nobelium Joining Gdańsk Tech Research Community - 'Excellence Initiative - Research University' program, Romney Meek and Franciszek Sikba for help with measurements and laser-induced porous graphene synthesis, respectively. The author (S.G.) is also thankful to M. Gazda and M. Łapiński (Gdańsk University of Technology), W. Nogala (IPC-PAN), N. Dimakis (University of Texas-Rio Grande Valley), and the anonymous reviewers for their valuable feedback on the peer review, which improved the manuscript.

Author contributions

S.G. contributed to the conception and design of the experiment, conducted synthesis of materials, prepared the devices, wrote the experimental part, performed data curation and analysis, performed performance measurements, and wrote the manuscript. M.N. and M.S. performed structural measurements, data curation, wrote the experimental part, and wrote the manuscript. R. B. contributed to part writing and editing of the manuscript.

Declarations

Competing financial interests, the authors declare no competing interests.

Additional information

Correspondence and requests for materials should be addressed to S.G.

Supplementary information is included in this paper.

Data Availability The datasets used and/or analyzed during the current study are available from the corresponding author on reasonable request.

Figure Captions

Fig. 1. Synthesis and morphological characterization. (a) Schematic of laser-induced porous graphene (LIPG) synthesis on polyimide (PI) film (50 micron thick). Representative (b, d) scanning electron microscopy and (c, e) transmission electron microscopy images at various magnifications revealing surface morphology and carbon phases for LIPG and GFNs (Gr, GO, CerGO, GA and NGA). Scale bars are shown at the bottom of the images.

Fig. 2. Structural Characterization. (a) X-ray diffractogram (b) Micro-Raman spectra showing characteristic peaks related to LIPG (c) High resolution X-ray photoelectron spectra showing different C-C and C-O chemical bonding including survey spectra (inset) showing C-N bonding and (d) Micro-Raman spectra of GFNs along with intensity ratio (I_D/I_G).

Fig. 3. Electrochemical properties of GFN electrodes. (a) Cyclic voltammograms with varying scan rate ($5\text{--}200\text{ mV s}^{-1}$) in macroelectrode configuration with 2.5mM potassium ferro/ferricyanide redox mediator with base electrolyte 0.5M Na_2SO_4 showing redox peaks. (b) Corresponding cathodic (I_{pc}) and anodic (I_{pa}) peak current = $f(\text{scan rate})^{1/2}$ behavior. (c) electrochemical impedance spectra measured at open circuit potential with (inset) equivalent RC circuit for LIPG and (d) cyclic voltammograms with scan rate ($5\text{--}500\text{ mV s}^{-1}$) in base electrolyte without redox probe for representative GFNs (LIPG, Gr, GO, CerGO, GA, NGA) in the non-faradic region to obtain the double-layer capacitance (C_{dl}).

Fig. 4. SECM characterization of GFNs. Cyclic voltammograms of (a) LIPG at two different z-position and (b) GO, rGO, GA and NGA, at scan rate 20 mV/s in microelectrode configuration. Probe approach curves in feedback mode showing variation of tip current versus distance behavior with tip voltage $V_t = +0.2\text{ V}$ for (c) LIPG at three different z-position in base electrolyte 0.1M KCl and 1mM Ferrocene methanol (FcMeOH) redox probe and (d) GFNs (GO, CerGO, ErGO, GA, NGA) in base electrolyte 0.5M Na_2SO_4 and 2.5mM $\text{K}_4\text{Fe}(\text{CN})_6/\text{K}_3\text{Fe}(\text{CN})_6$ redox probe, along with Cornut and Lefrou fit.

Fig. 5. SECM imaging electroactivity. (a) SECM images over $500 \times 500\text{ }\mu\text{m}^2$ area for LIPG electrode surface at two different z-position and area locations under tip voltage $V_t = +0.5\text{ V}$, substrate voltage $V_s = 0\text{ V}$ and (b) SECM images over $600 \times 600\text{ }\mu\text{m}^2$ area for GFNs (Gr, GO, rGO, GA and NGA) under tip voltage $V_t = +0.4\text{ V}$ and substrate voltage $V_s = 0\text{ V}$ conditions, displaying probe current distribution as two-dimensional contour map and three-dimensional “heat maps” with occasional higher/lower current behavior.



Fig. 6. Quantifying structure-property-electroactivity relationships. (a) Variation of defects number density (n_D) and inter-defect distance (L_D) via micro-Raman spectra correlated with k_{ET} (or k_{eff}) via SECM alongside k^0 from Nicholson method for GFNs (Gr, Gr_{def}, GO, CerGO, rGO_{th}, ErGO, GA, NGA, LIPG). The error bars represent the standard deviation in deducing the defect density using 7–8 points Raman spectra and the uncertainty in probe approach curve fitting. (b) Schematic for versatility of defects (intrinsic, basal plane) and imperfections (edge plane sites, oxygenated functional groups, nitrogen dopants) in graphene-based electrodes impacting electron transfer kinetics rate.

Fig. 7. Theoretical calculations of electronic structure with defects and dopant. (*left*) Model schematics of DFT optimized structures of (a) defective graphene with 1C (one), 2C (two non-adjacent), and 4C (four adjacent) vacancies in non-hydrated and hydrated conditions and (b) graphene oxide (GO; O/C=37.5%), reduced GO (rGO; O/C=12.5%), N-rGO (rGO configuration with N adjacent to C and N) and nitrogen doped graphene (NGA; N/C=12.5%). For H₂O/graphene without defects, $h_0 = 3.04\text{\AA}$. The rectangle shows the periodic cell. Atoms are colored as follows: C, gray; H, white; N, blue; O, red. (*right*) Corresponding density of states (DOS) spectra per carbon atom for the structures shown in (a) and (b). The vertical dash line is the Fermi energy (E_F). For (b) the Direct point E_D relative to the E_F is shown. When band gaps are observed, the bandgap values (E_g) are shown.

Fig. 8. Energy level alignment scheme and effects of overpotential on k_{ET} . (a) The total capacitance of graphene electrode/electrolyte interface. (b) Density and occupation of states in the uncharged/un-electrified graphene layer. (c) The distribution and occupation of redox molecular states in solution. The alignment of Fermi levels in the (d) classical limit (e) quantum limit and (f) mixed case (adapted from [143]). (g) Schematic of the anticipated EDL capacitance of pristine, defective and N-doped graphene with operating potential window. (h) Effect of double-layer capacitance ($C_{EDL} = 2$ and $5\text{ }\mu\text{F}/\text{cm}^2$) on the dependence of ET rate constant on the standard potential V^0 for pristine graphene (Gr) and defective graphene with monovacancy (Gr_{def}). (i) Dependence of ET rate constant of Gr_{def} on standard redox potential V^0 . The standard potentials for typical one-electron redox couples are depicted by vertical lines [155].

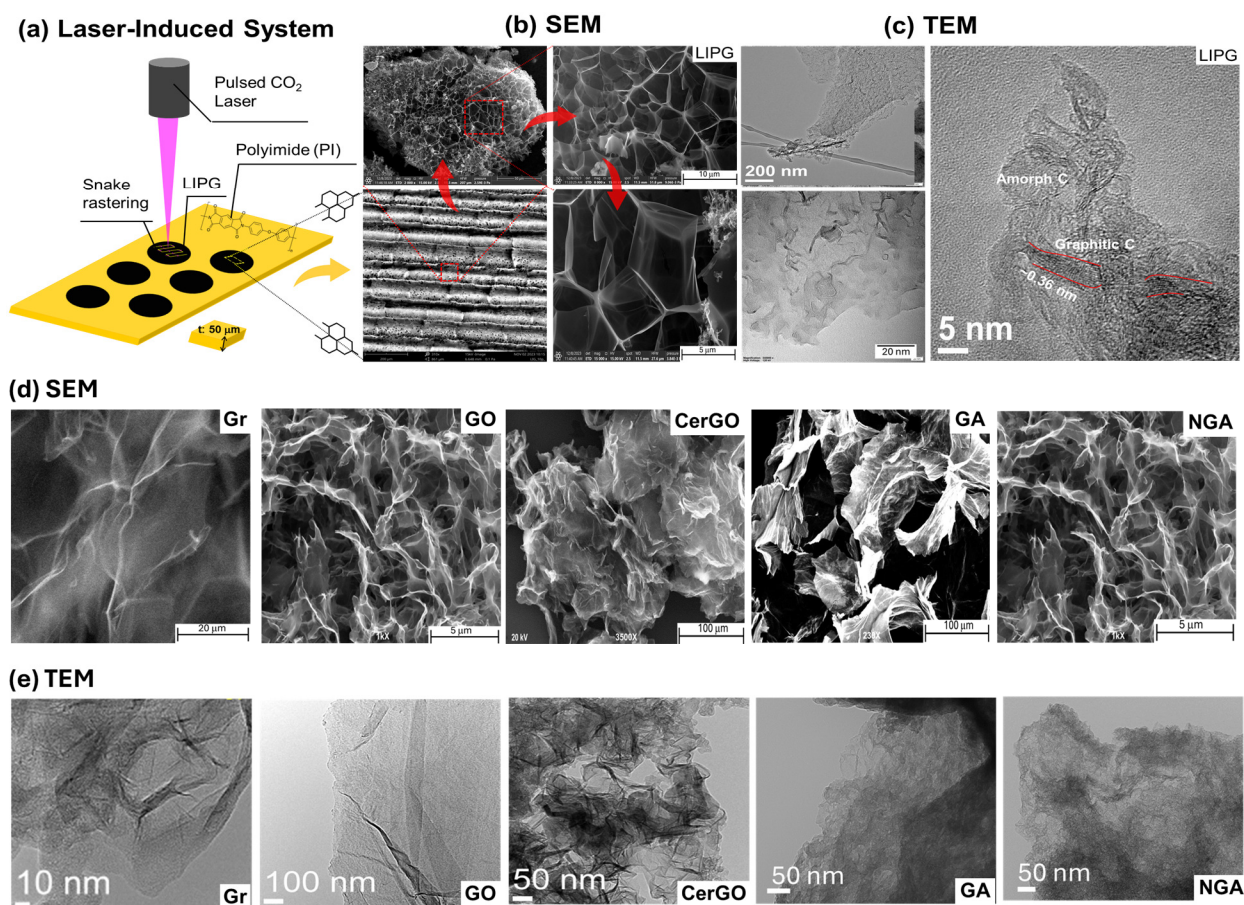


Fig. 1. Synthesis and morphological characterization. (a) Schematic of laser-induced porous graphene (LIPG) synthesis on polyimide (PI) film (50 micron thick). Representative (b, d) scanning electron microscopy and (c, e) transmission electron microscopy images at various magnifications revealing surface morphology and carbon phases for LIPG and GFNs (Gr, GO, CerGO, GA and NGA). Scale bars are shown at the bottom of the images.

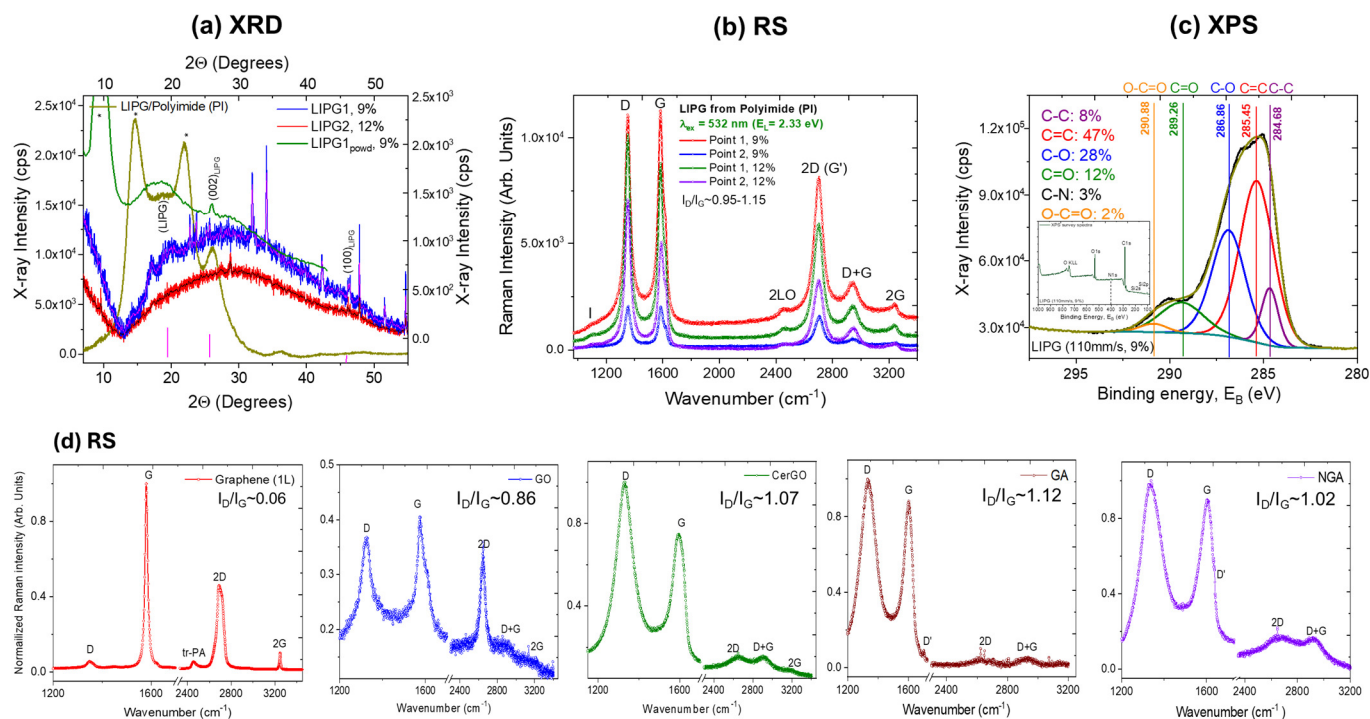


Fig. 2. Structural Characterization. (a) X-ray diffractogram (b) Micro-Raman spectra showing characteristic peaks related to LIPG (c) High resolution X-ray photoelectron spectra showing different C-C and C-O chemical bonding including survey spectra (inset) showing C-N bonding and (d) Micro-Raman spectra of GFNs along with intensity ratio (I_D/I_G).

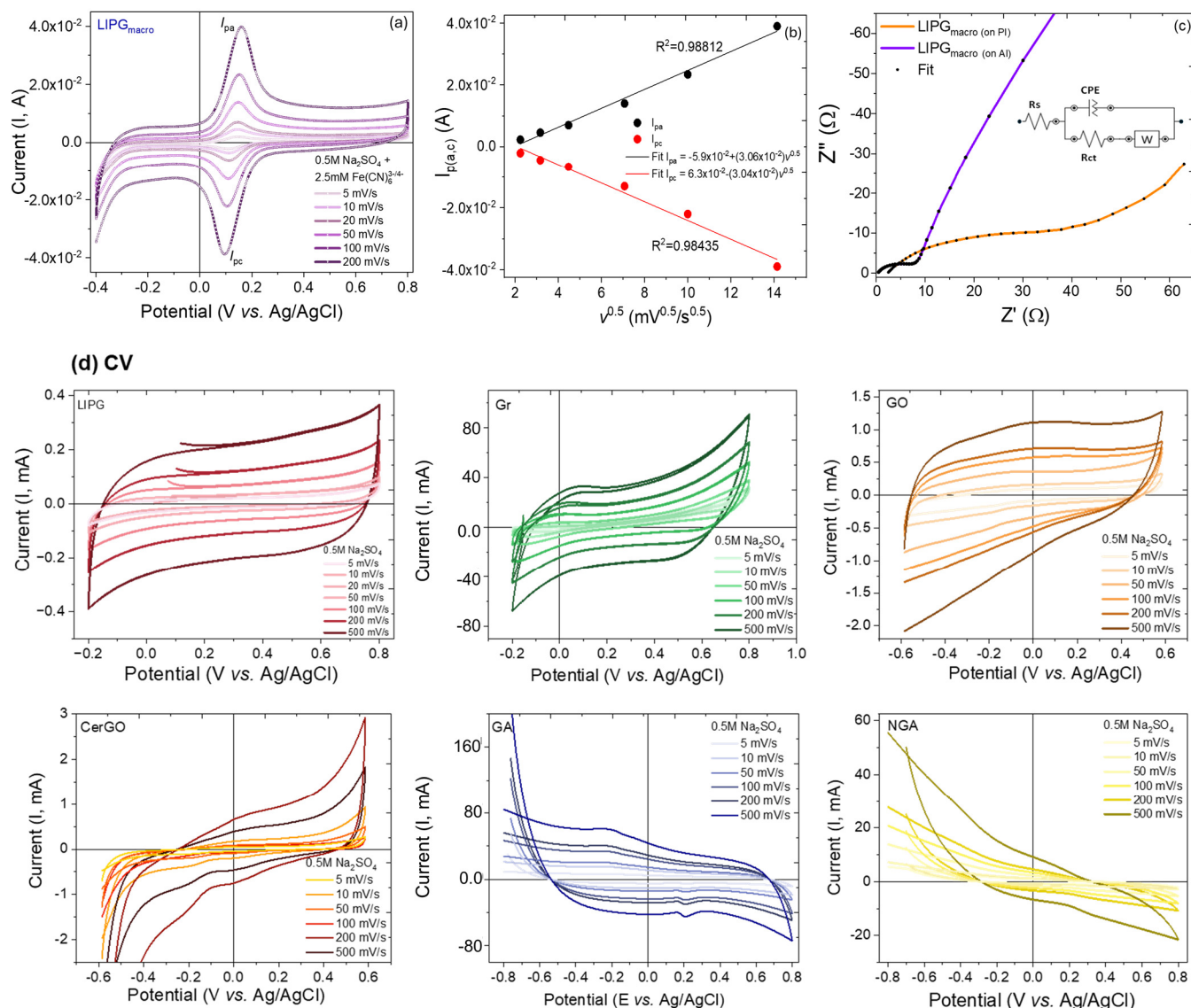


Fig. 3. Electrochemical properties of GFN electrodes. (a) Cyclic voltammograms with varying scan rate (5–200 mV s⁻¹) in macroelectrode configuration with 2.5mM potassium ferro/ferricyanide redox mediator with base electrolyte 0.5M Na₂SO₄ showing redox peaks. (b) Corresponding cathodic (I_{pc}) and anodic (I_{pa}) peak current = $f(\text{scan rate})^{1/2}$ behavior. (c) electrochemical impedance spectra measured at open circuit potential with (inset) equivalent RC circuit fit for LIPG and (d) cyclic voltammograms with scan rate (5–500 mV s⁻¹) in base electrolyte without redox probe for representative GFNs (LIPG, Gr, GO, CerGO, GA, NGA) in the non-faradic region to obtain the double-layer capacitance (C_{dl}).

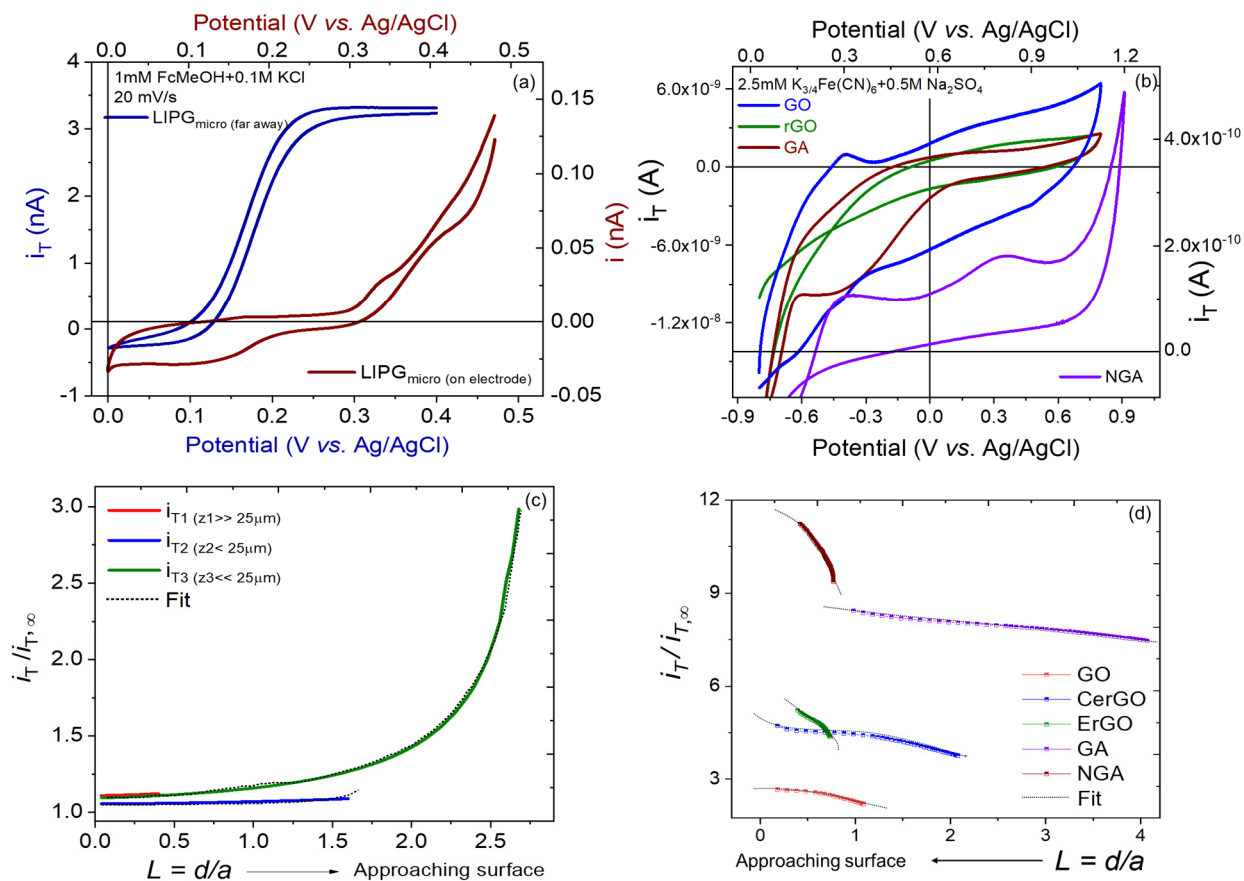


Fig. 4. SECM characterization of GFNs. Cyclic voltammograms of (a) LIPG at two different z-position and (b) GO, rGO, GA and NGA, at scan rate 20 mV/s in microelectrode configuration. Probe approach curves in feedback mode showing variation of tip current versus distance behavior with tip voltage $V_t = +0.2$ V for (c) LIPG at three different z-position in base electrolyte 0.1M KCl and 1mM Ferrocene methanol (FcMeOH) redox probe and (d) GFNs (GO, CerGO, ErGO, GA, NGA) in base electrolyte 0.5M Na_2SO_4 and 2.5mM $K_4Fe(CN)_6$ / $K_3Fe(CN)_6$ redox probe, along with Cornut and Lefrou fit.

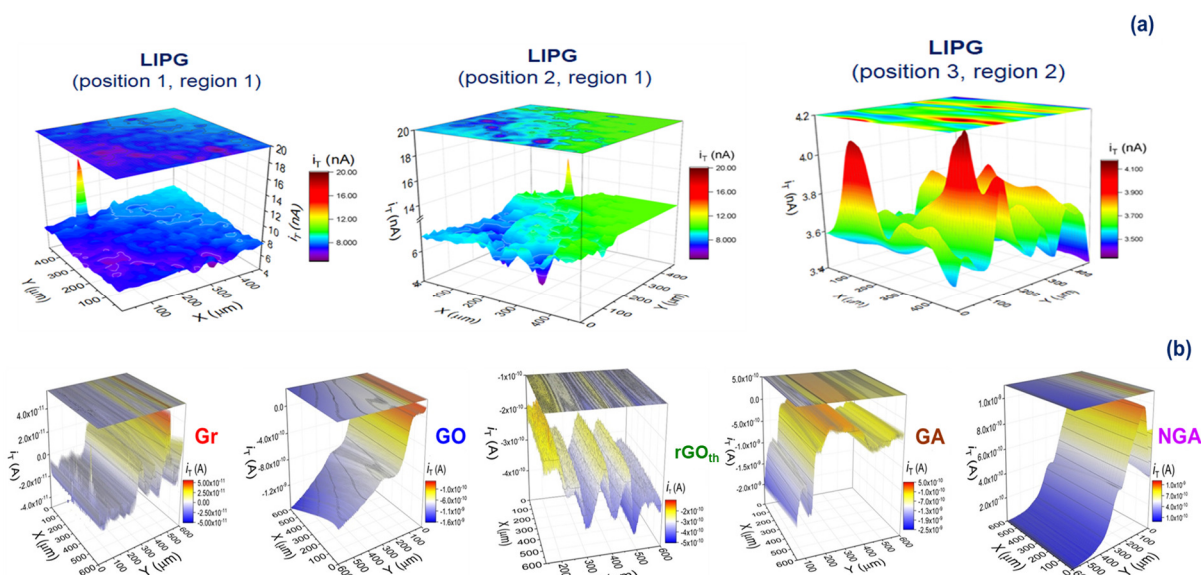


Fig. 5. SECM imaging electroactivity. (a) SECM images over $500 \times 500 \mu\text{m}^2$ area for LIPG electrode surface at two different z-position and area locations under tip voltage $V_t = +0.5 \text{ V}$, substrate voltage $V_s = 0 \text{ V}$ and (b) SECM images over $600 \times 600 \mu\text{m}^2$ area for GFNs (Gr, GO, rGO_{th}, GA and NGA) under tip voltage $V_t = +0.4 \text{ V}$ and substrate voltage $V_s = 0 \text{ V}$ conditions, displaying probe current distribution as two-dimensional contour map and three-dimensional “heat maps” with occasional higher/lower current behavior.

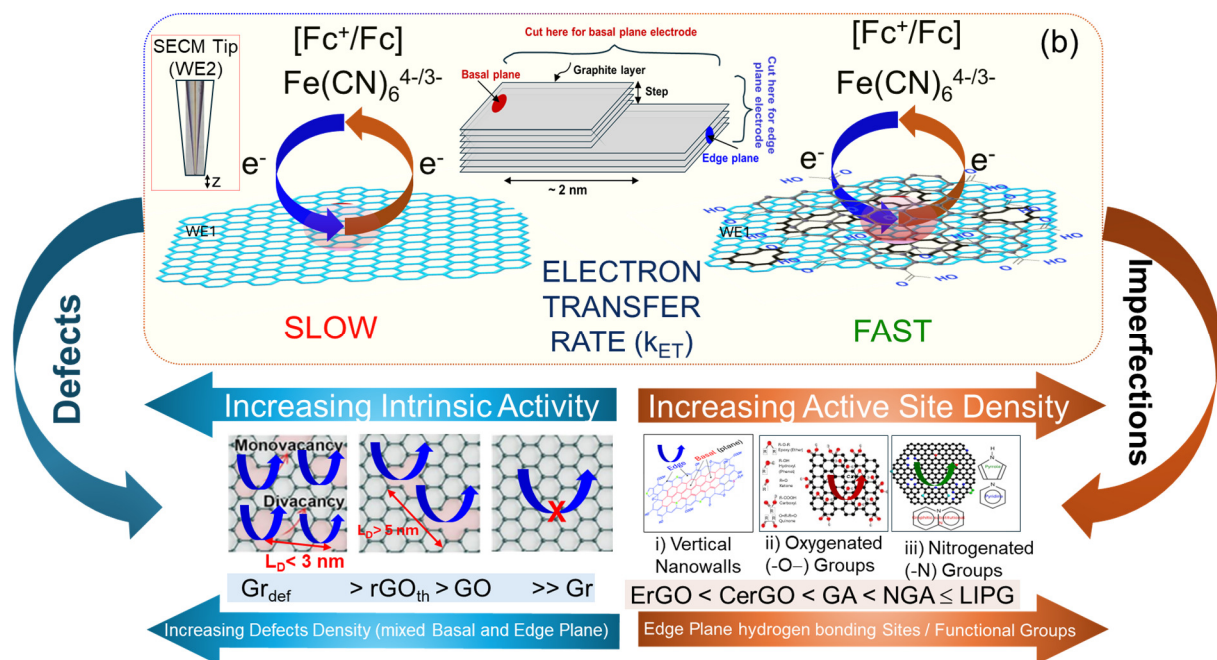
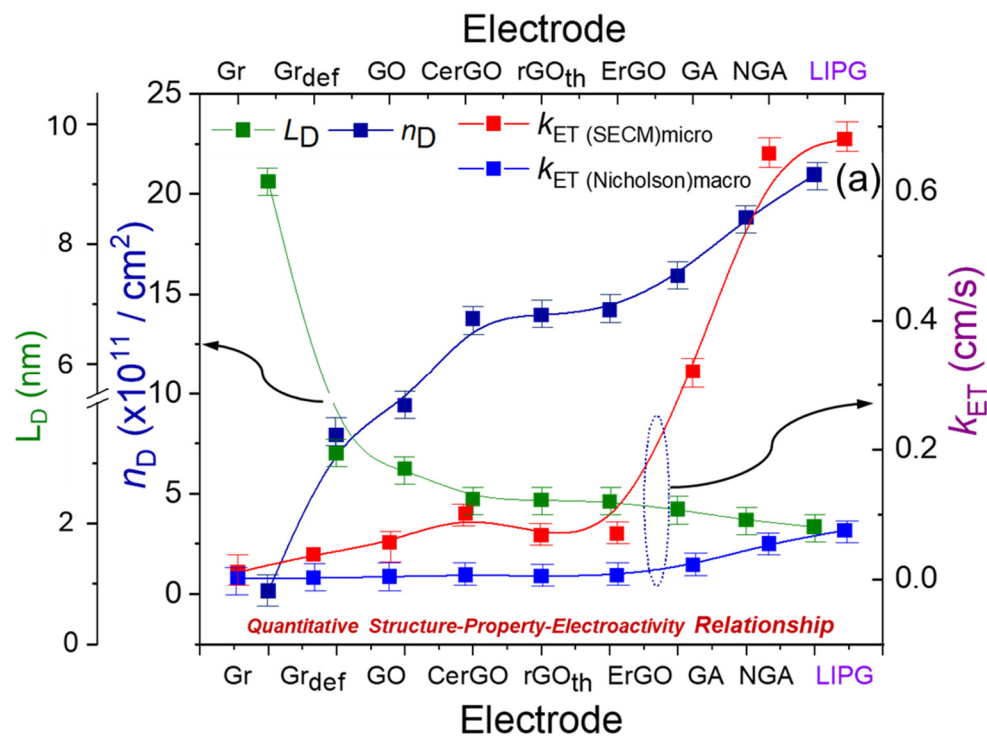


Fig. 6. Quantifying structure-property-electroactivity relationships. (a) Variation of defects number density (n_D) and inter-defect distance (L_D) via micro-Raman spectra correlated with k_{ET} (or k_{eff}) via SECM alongside k^0 from Nicholson method for GFNs (Gr, Gr_{def}, GO, CerGO, rGO_{th}, ErGO, GA, NGA, LIPG). The error bars represent the standard deviation in deducing the defect density using 7–8 points Raman spectra and the uncertainty in probe approach curve fitting. (b) Schematic for versatility of defects (intrinsic, basal plane) and imperfections (edge plane sites, oxygenated functional groups, nitrogen dopants) in graphene-based electrodes impacting electron transfer kinetics rate.

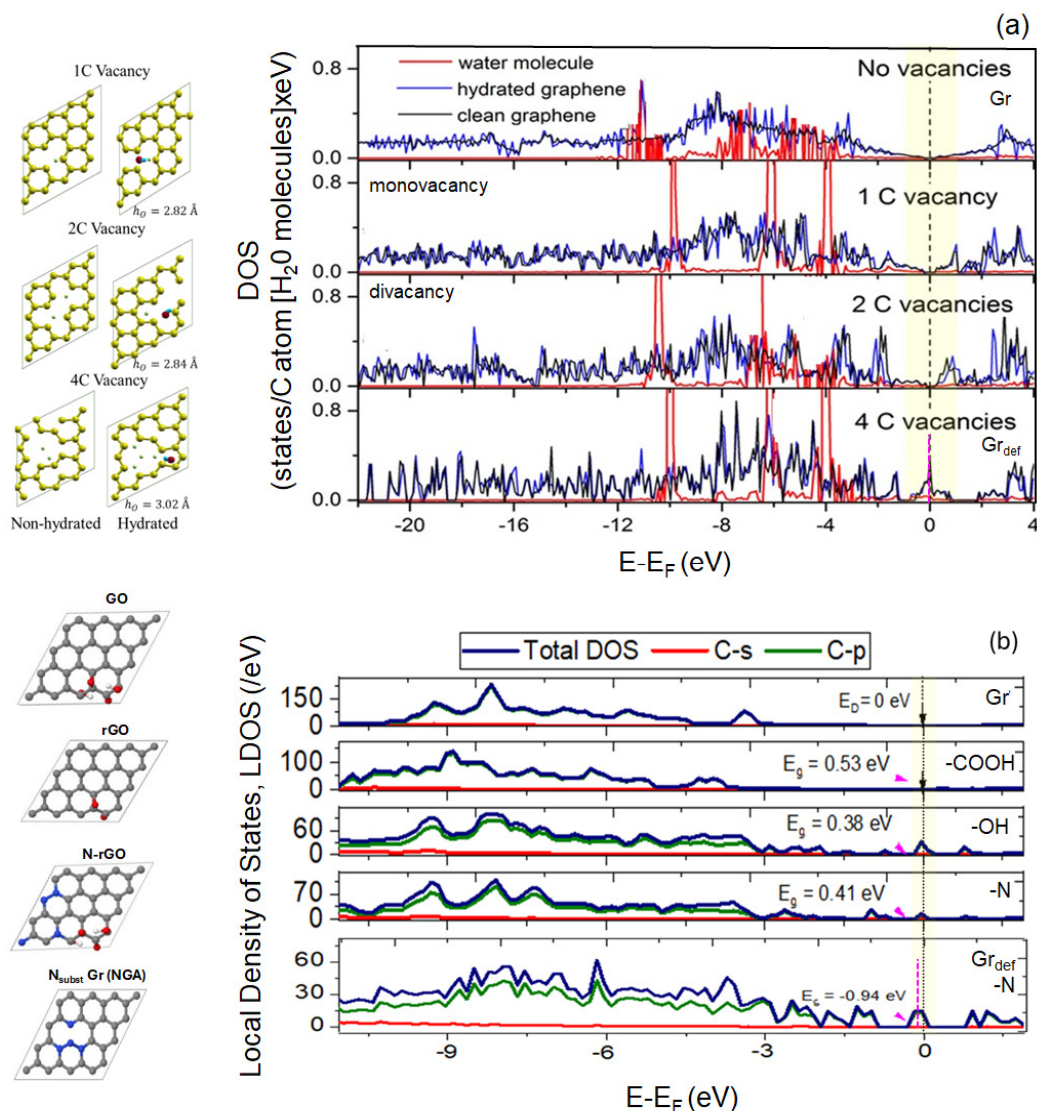


Fig. 7. Theoretical calculations of electronic structure with defects and dopant. (left) Model schematics of DFT optimized structures of (a) defective graphene with 1C (one), 2C (two non-adjacent), and 4C (four adjacent) vacancies in non-hydrated and hydrated conditions and (b) graphene oxide (GO; O/C=37.5%), reduced GO (rGO; O/C=12.5%), N-rGO (rGO configuration with N adjacent to C and N) and nitrogen doped graphene (NGA; N/C=12.5%). For H_2O /graphene without defects, $h_0 = 3.04 \text{ \AA}$. The rectangle shows the periodic cell. Atoms are colored as follows: C, gray; H, white; N, blue; O, red. (right) Corresponding density of states (DOS) spectra per carbon atom for the structures shown in (a) and (b). The vertical dash line is the Fermi energy (E_F). For (b) the Direct point E_D relative to the E_F is shown. When band gaps are observed, the bandgap values (E_g) are shown.

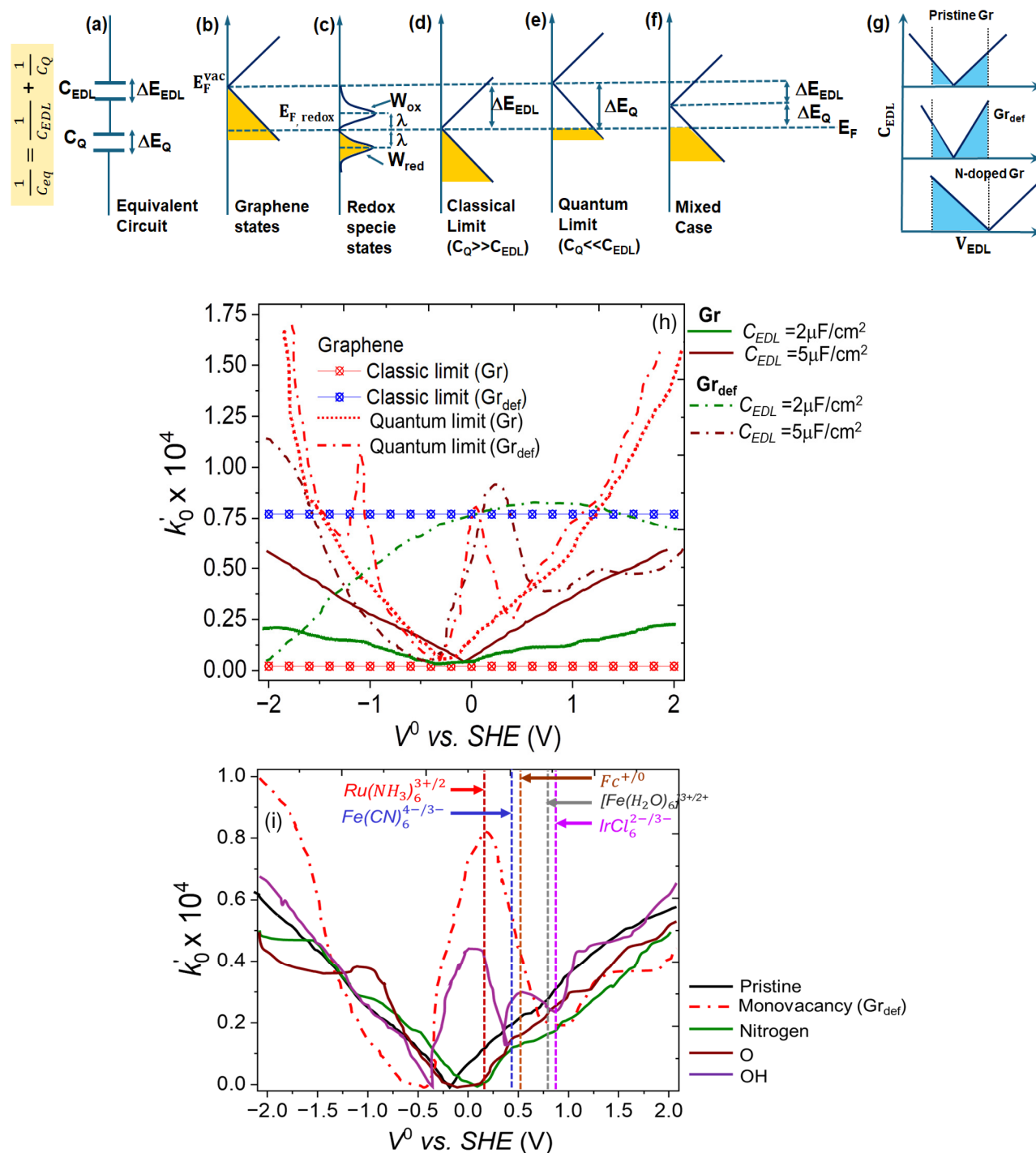


Fig. 8. Energy level alignment scheme and effects of overpotential on k_{ET} . (a) The total capacitance of graphene electrode/electrolyte interface. (b) Density and occupation of states in the uncharged/un-electrified graphene layer. (c) The distribution and occupation of redox molecular states in solution. The alignment of Fermi levels in the (d) classical limit (e) quantum limit and (f) mixed case (adapted from [143]). (g) Schematic of the anticipated EDL capacitance of pristine, defective and N-doped graphene with operating potential window. (h) Effect of double-layer capacitance ($C_{EDL} = 2$ and $5 \mu\text{F}/\text{cm}^2$) on the dependence of ET rate constant on the standard potential V^0 for pristine graphene (Gr) and defective graphene with monovacancy (Gr_{def}). (i) Dependence of ET rate constant of Gr_{def} on standard redox potential V^0 . The standard potentials for typical one-electron redox couples are depicted by vertical lines [155].

Table 1. Summary of electrochemical active surface area derived from the obtained C_{dl} values for graphene-family nanomaterial electrodes. The geometric surface area (A) of electrode immersed in electrolyte was 0.125 cm^2 (or 0.196 cm^2).

Electrode	$C_{dl} \text{ (mF/cm}^2\text{)}$	Electrochemical active surface area, ECSA (cm^2)
Defective (Gr_{def})	0.62 ± 0.05	$38.8 \text{ (60.8)} \pm 2.01$
GO	2.3 ± 0.10	57.2 ± 2.53
CerGO (/rGO)	3.5 ± 0.10	87.5 ± 2.65
rGO_{th}	3.8 ± 0.15	95.0 ± 3.17
GA	9.5 ± 0.21	237.5 ± 4.68
NGA	10.7 ± 0.25	267.5 ± 5.85
LIPG	11.2 ± 0.25	280.0 ± 5.93

Table 1.
Gupta *et. al.*,

Table 2. Summary of electrochemical impedance spectroscopy parameters fitted with CPE equivalent circuit elements and graphical method for graphene-family nanomaterial electrodes.

Electrode	R_s (Ω)	α	R_{ct} (Ω)	Q (F)	Z_w (Ω)	C_{eff} (mF/cm ²) @1-10Hz	Fitting Error (%)
Defective (Gr _{def})	6.481±.14	0.832±.016	0.886±.023	0.0056±.0013	2.573±.017	0.54±.01	2.7
GO	6.573±.13	0.841±.017	1.251±.014	0.0035±.0010	2.988±.016	2.1±.01	2.3
CerGO	6.782±.10	0.845±.015	1.052±.021	0.0065±.0012	2.732±.010	3.6±.04	2.6
rGO _{th}	6.465±.16	0.853±.014	1.103±.017	0.0052±.0017	2.345±.011	3.7±.03	3.3
GA	6.796±.15	0.869±.012	0.824±.025	0.045±.0020	1.433±.012	8.9±.06	2.1
NGA	6.684±.12	0.871±.015	0.873±.031	0.025±.0019	1.485±.011	9.3±.08	2.8
LIPG	6.883±.11	0.868±.013	0.775±.024	0.036±.0016	1.567±.015	10.8±.09	3.2

Note: R_s is the uncompensated electrolyte solution resistance.

α is the constant phase element exponent associated with extent of electrochemical double-layer capacitance at the electrode-electrolyte interface.

R_{ct} is the charge transfer resistance between the interface of electrode and electrolyte.

Q is the constant phase element exponent associated with electrochemical double-layer capacitance at the electrode-electrolyte interface.

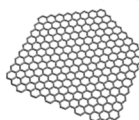
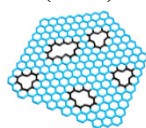
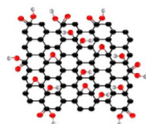
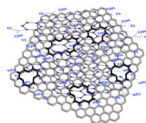
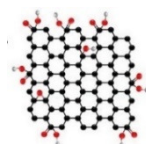
Z_w is the Warburg impedance associated with impedance in the low frequency region.

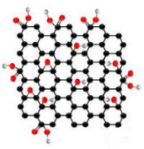
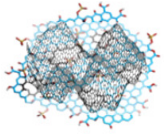
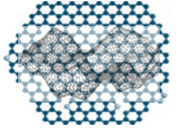
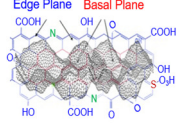
The errors mentioned represent uncertainties and a relatively standard fit error.

Table 2.
Gupta *et. al.*,



Table 3. Comparison of electron transfer kinetic rate constant values determined using macroelectrode (Traditional) and microelectrode (SECM) configurations across graphene-family nanomaterial electrodes.

Electrode	k^0 (Nicholson) (cm/s)	k_{app} (from R_{ct}) (cm/s)	k_{eff} (Cornut and Lefrou) ^{a,b} (cm/s)	k_{ET} or k_{eff} (Empirical k_1) ^a (cm/s)	Validity range (μm) and χ^2 (% Error)
	Macroelectrode (averaged)		Microelectrode (smaller ensemble)		
Monolayer Graphene Pristine (Gr)  Defective (Gr _{def}) 	1.05×10 ⁻³	0.9×10 ⁻³	(1.11±0.2)×10 ⁻²	(1.5±0.2)×10 ⁻²	10 μm (< 1)
	1.9×10 ⁻³	5.3×10 ⁻³	(3.8–5.5±0.5)×10 ⁻²	(5.6–6.7±0.2)×10 ⁻²	
GO 	3.8×10 ⁻³	4.5×10 ⁻³	(5.63±0.2)×10 ⁻²	(8.2±0.2)×10 ⁻²	10 μm (< 1)
CerGO 	6.9×10 ⁻³	7.3×10 ⁻³	(10.01±0.2)×10 ⁻²	(11.12±0.2)×10 ⁻²	10 μm (< 1)
rGO_{th} 	4.9×10 ⁻³	6.8×10 ⁻³	(6.87±0.2)×10 ⁻²	(5.97±0.2)×10 ⁻²	10 μm (< 1)

ErGO 	5.9×10^{-3}	6.4×10^{-3}	$(6.69 \pm 0.5) \times 10^{-2}$	$(5.49 \pm 0.5) \times 10^{-2}$	10 μm (< 1)
GA 	2.21×10^{-2}	3.43×10^{-2}	$(3.21 \pm 0.5) \times 10^{-1}$	$(2.87 \pm 0.5) \times 10^{-1}$	10 μm (< 1)
NGA 	5.50×10^{-2}	3.91×10^{-2}	$(6.58 \pm 0.5) \times 10^{-1}$	$(6.45 \pm 0.5) \times 10^{-1}$	10 μm (< 1)
LIPG 	7.54×10^{-2}	3.84×10^{-2}	$(6.79 \pm 0.5) \times 10^{-1}$	$(6.42 \pm 0.5) \times 10^{-1}$	20 μm (< 1)

^a $V_t = +0.4\text{V}$ (or $+0.5\text{V}$), $V_s = 0\text{V}$. ^b Errors represent the uncertainty in fitting k_{eff} .

Table 3.
Gupta *et. al.*,

Electronic Supporting Information (ESI)

Perspectives on Electron Transfer Kinetics Across Graphene-Family Nanomaterials and Interplay of Defects, Electronic Structure, and Quantum Capacitance

Sanju Gupta^{a,b,c}, Magdalena Narajczyk^d, Mirosław Sawczak^e, Robert Bogdanowicz^{a,b}

^a Department of Metrology and Optoelectronics, Faculty of Electronics, Telecommunication and Informatics, Gdansk University of Technology, Narutowicza Str. 11/12, 80-233 Gdansk, Poland

^b Advanced Materials Center, Gdansk University of Technology, 80-233 Gdansk, Poland

^c Department of Physics, Pennsylvania State University, University Park, PA 16802 (USA)

^d Faculty of Biology, University of Gdansk, Wita Stwosza 59, 80-308 Gdansk, Poland

^e The Szewalski Institute of Fluid-Flow Machinery, Polish Academy of Sciences, Fiszerza 14, 80-231 Gdansk, Poland

Synthesis Scheme

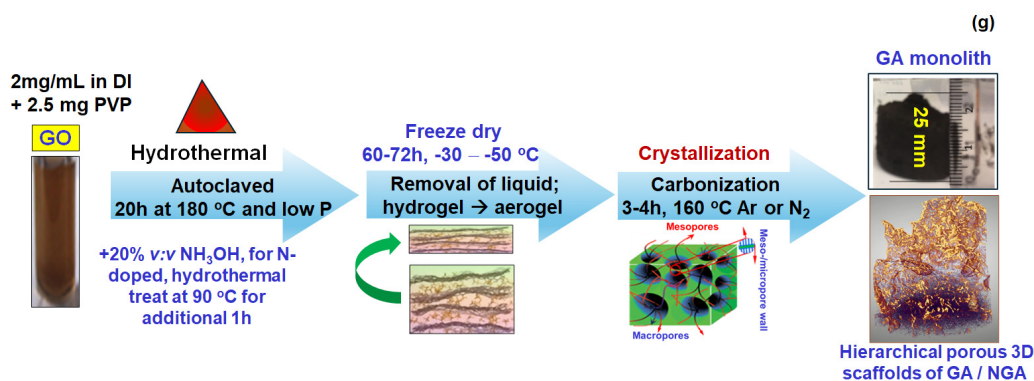
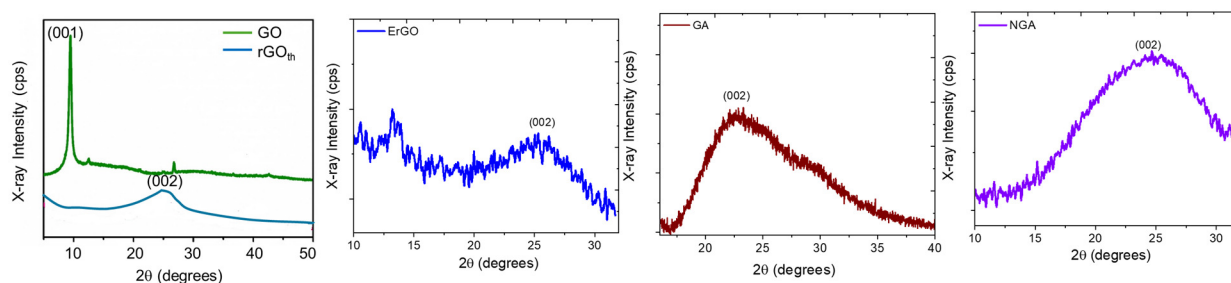


Figure S1. Hydrothermal approach to synthesizing GA and NGA monoliths.



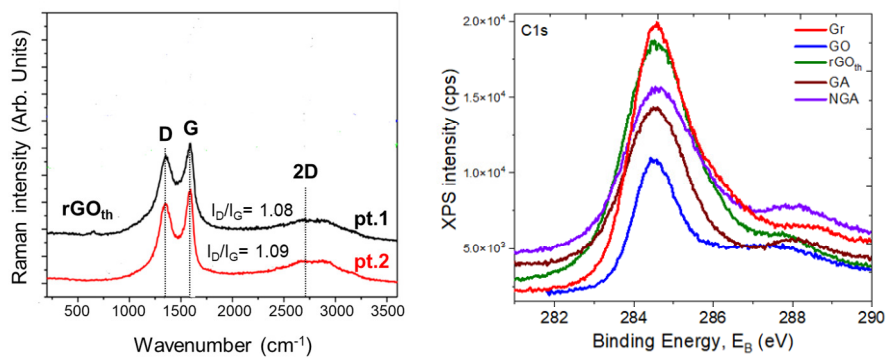


Figure S2. XRD of thermally reduced graphene oxide (rGO_{th}) along with GO precursor for comparison, ErGO, GA and NGA showing characteristic diffraction peak. Also shown are Raman spectra of rGO_{th} at two different points showing Raman bands and high-resolution XPS spectra.

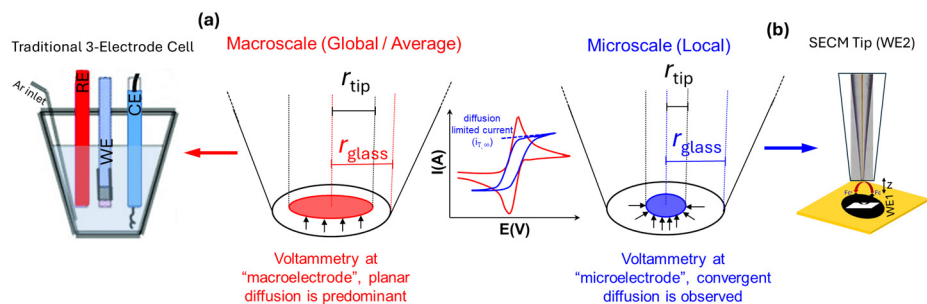


Figure S3. Macroscale and microscale electrochemistry. (a) Traditional electrochemical cell with “macroelectrode” (one working electrode, WE) and (b) Tip-based SECM with “microelectrode” configuration (two working electrodes, WE1 and WE2), revealing planar and convergent diffusion behavior, respectively. Also shown are the typical voltammetry profiles from these two methods.

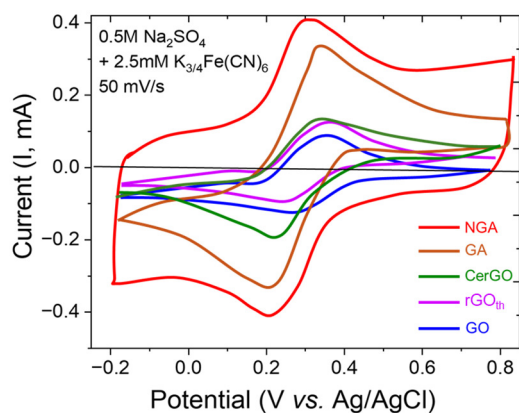


Figure S4. Cyclic voltammogram of GFNs with redox probe showing the cathodic and anodic peaks.

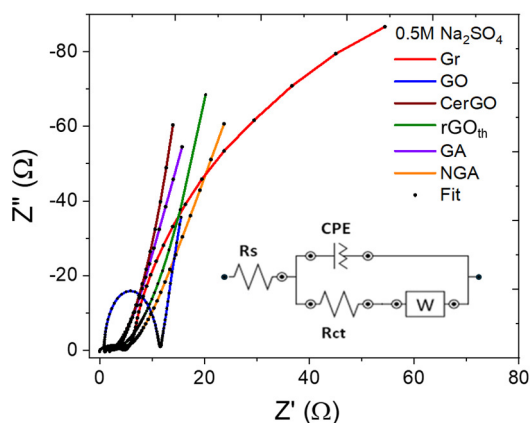


Figure S5. EIS data (solid) measured at OCP (~100 mV or 0.1V) and fitting with CPE equivalent circuit shown in inset for GFNs (Gr, GO, CerGO, rGO_{th}, GA, NGA).

S5: Fitting of steady-state SECM approach curves with finite first-order kinetics (k_1) at the electrode surface and diffusion-controlled kinetics at the microelectrode

Normalized heterogeneous rate constants κ have been extracted from experimental approach curves by fitting them to an analytical approximation of simulated data evaluated following Cornut and Lefrou fit accepting the procedure described below [157].

Input parameters

The radius of the active part of the microelectrode, r_{tip} , the ratio of the insulating glass sheath r_{glass} and r_{tip} , known as RG , and the point of closest approach d_0 have been determined from independent experiments. RG was determined by optical microscopy; r_{tip} and d_0 were determined from probe approach curves to insulating glass and fitting them to theoretical curves proposed by Amphlett and Denuault [158].

Probe approach curves fitting

Experimental probe approach profiles *i.e.*, $i_T(z)$ was normalized with steady-state i_T at large z or $i_{T,\infty} = 4nFDr_{\text{tip}}c^*\beta(RG)$. Current i_T and distance L have been calculated using Eqs. (S1-1) and (S1-2) or Eq. (S1-3). Eq. (S1-2) applies for increasing piezo position z (\uparrow) for decreasing (\downarrow) microelectrode-to-sample electrode surface d (Fig. S1A). Eq. (S1-3) applies for decreasing z for decreasing d (Fig. S1B).

$$I_T = i_T / i_{T,\infty} \quad (\text{S1})$$

$$L = z - z_{\text{offset}} / -r_{\text{tip}} \quad (\text{S2})$$

$$L = z - z_{\text{offset}} / r_{\text{tip}} \quad (\text{S3})$$

z_{offset} is calculated according to Eqs. (S1-4) and (S1-5) which correspond to case A or B, respectively. d_0 is the distance of the active microelectrode area to the sample electrode when the insulating sheath touches the surface.

$$z_{\text{offset}} = \max(z) + d_0 \quad (\text{S4})$$

$$z_{\text{offset}} = \min(z) - d_0 \quad (\text{S5})$$

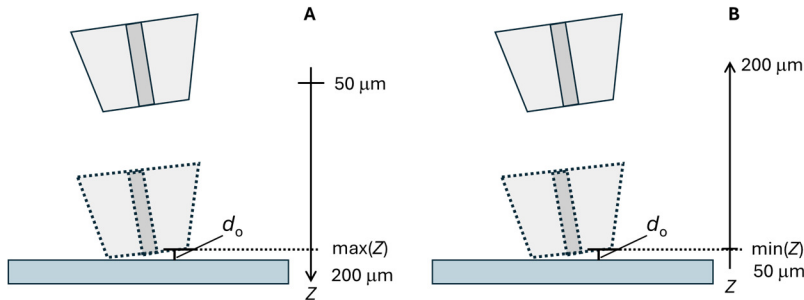


Figure S6. Determination of z_{offset} and L for (A) increasing z for decreasing d and (B) decreasing z for decreasing d .

The analytical approximation of Cornut and Lefrou [Error! Bookmark not defined.] was used for calculating a theoretical current I_T for each experimental, normalized distance L (typically shown as $d/a = z / r_{\text{tip}}$).

$$I_T(L, \kappa, RG) = I_T^{\text{cond}}\left(L + \frac{1}{\kappa}, RG\right) + \frac{I_T^{\text{ins}}(L, RG) - 1}{(1 + 2.47RG^{0.31}L\kappa)(1 + L^{0.006RG + 0.1113\kappa - 0.0236RG + 0.91})} \quad (\text{S6})$$

with

$$I_T^{\text{cond}}\left(L + \frac{1}{\kappa}, RG\right) = \alpha(RG) + \frac{1}{2\beta(RG)\xi\left(L + \frac{1}{\kappa}\right)} + \left(1 - \alpha(RG) - \frac{1}{2\beta(RG)}\right)\xi\left(L + \frac{1}{\kappa}\right) \quad (\text{S7})$$

$$I_T^{\text{ins}}(L, RG) = \frac{\frac{2.08}{RG^{0.358}}\left(L - \frac{0.145}{RG}\right) + 1.585}{\frac{2.08}{RG^{0.358}}(L + 0.0023RG) + 1.57 + \frac{\ln RG}{L} + \frac{2}{\pi RG} \ln\left(1 + \frac{\pi RG}{2L}\right)} \quad (\text{S8})$$

$$\alpha(RG) = \ln 2 + \ln 2 \left(1 - \frac{2}{\pi} \arccos\left(\frac{1}{RG}\right)\right) - \ln 2 \left(1 - \left(\frac{2}{\pi} \arccos\left(\frac{1}{RG}\right)\right)^2\right) \quad (\text{S9})$$

$$\beta(RG) = 1 + 0.639 \left(1 - \frac{2}{\pi} \arccos\left(\frac{1}{RG}\right)\right) - 0.186 \left(1 - \left(\frac{2}{\pi} \arccos\left(\frac{1}{RG}\right)\right)^2\right) \quad (\text{S10})$$

$$\xi\left(L + \frac{1}{\kappa}\right) = \frac{2}{\pi} \arctan\left(L + \frac{1}{\kappa}\right) = \frac{2}{\pi} \tan^{-1}\left(L + \frac{1}{\kappa}\right) \quad (\text{S11})$$

$$\kappa = \frac{k_{\text{eff}} r_{\text{tip}}}{D} \quad (\text{S12})$$

$\beta(RG) \sim 1.02$, for $RG=10$ and $\beta(RG) \sim 1.01$, for $RG=25$. Note that k_{eff} is also labelled as k_{ET} or k^0 (cm/s) in the literature.

κ , $i_{T,\infty}$, and d_0 (within reasonable range which is ~ 10 microns) were varied to fit the experimental approach curves.

Heterogeneous rate constant k_{eff} was calculated from κ .

$$k_{\text{eff}} = \frac{\kappa D}{r_{\text{tip}}} \quad (\text{S13})$$

As for the empirical approach [70], the corresponding probe approach curves fitting can also determine L and corresponding kinetic rate constant κ (or k_{ET}) from the following:

$$I_T^{\text{cond}}(L) = \frac{0.78377}{L} + 0.68 + 0.3315 \exp\left(-\frac{1.0672}{L}\right) \quad (\text{S14})$$

$$I_T^{ins}(L) = \frac{1}{\frac{1.5358}{L} + 0.15 + 0.58 \exp\left(-\frac{1.14}{L}\right) + 0.0908 \exp((L - 6.3)/(1.017L))} \quad (S15)$$

S6: ET rate dependence upon overpotential.

To illustrate the influence of potential on how it influences the ET rate constant, we plot the integrands $f_o(E, \eta)$ and $f_R(E, \eta)$ of the oxidation and reduction rate constants k'_R and k'_R (see Eqs. (S14) and (S15) in main text) in Fig. S3:

$$f_o(E, \eta) = \exp\left\{-\frac{(E - E_{F, redox} + \lambda)^2}{4\lambda k_B T}\right\} (1 - f(E - E_F + |e|\eta)) \rho_G(E, \eta) \quad (S16)$$

$$f_R(E, \eta) = \exp\left\{-\frac{(E - E_{F, redox} + \lambda)^2}{4\lambda k_B T}\right\} (1 - f(E - E_F + |e|\eta)) \rho_G(E, \eta) \quad (S17)$$

η is the overpotential, $f(E)$ the Fermi-Dirac distribution, ρ_G the density of electronic states of the electrode, E_F the Fermi energy of electrode, $E_{F, redox}$ the electrochemical potential of electrons in solution.

Integrated areas at positive overpotential are larger than those at negative overpotential. Therefore, it leads to asymmetrical dependence of the rate constant $k'_R(\eta) + k'_R(\eta)$ relative to the point $\eta = 0$.

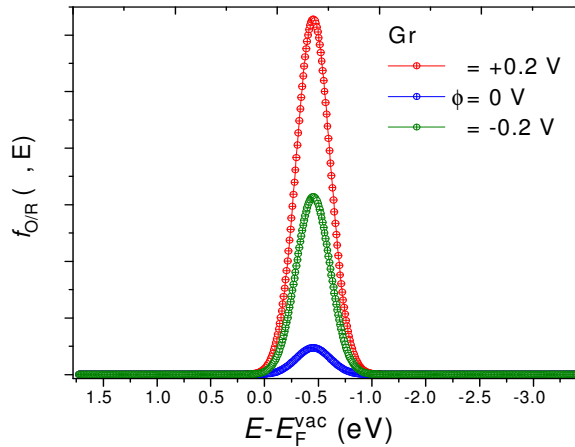


Figure S7. The integrands $f_o(E, \eta)$ and $f_R(E, \eta)$ at (a) $\eta = +0.2$ V (b) $\eta = 0$ V and (c) $\eta = -0.2$ V. Note that the standard potential E^0 for similar outer-sphere redox couples $\text{Fe}(\text{CN})_6^{3-/4-}$ and $\text{Fc}^{+/0}$ are 0.361 V and 0.40 V and the reorganization energy λ , eV is 0.83 and 0.85 eV, respectively.

References

- [1] J. U. Park, S. Nam, M. S. Lee, C. M. Lieber, Synthesis of monolithic graphene–graphite integrated electronics, *Nature Mater.* 11, 120–125 (2012).
- [2] A. K. Geim, Graphene: status and prospects, *Science* 324, 1530–1534 (2009).
- [3] S. Gupta, B. Evans, A. Henson, Graphene-based aerogels with carbon nanotubes as ultrahigh-performing mesoporous capacitive deionization electrodes for brackish and seawater desalination *Water Desal. Treat* 162, 97–111 (2019).
- [4] R. Kötz, M. Carlen, Principles and applications of electrochemical capacitors, *Electrochim. Acta*, 45, 2483–2498 (2000).
- [5] B. E. Conway, *Electrochemical Supercapacitor: Scientific Fundamentals and Technological Applications* (Plenum; New York, 1999).
- [6] N. Mohanty, V. Berry, Graphene-based single-bacterium resolution biodevice and DNA transistor: interfacing graphene derivatives with nanoscale and microscale biocomponents, *Nano Lett.* 8, 4469–4476 (2008).
- [7] Y. Shao, J. Wang, H. Wu, J. Liu, I. A. Aksay, Y. Lin, Graphene based electrochemical sensors and biosensors: a Review, *Electroanal.* 22, 1027–1036 (2010).
- [8] Y. Ohno, K. Maehashi, K. Matsumoto, Chemical and biological sensing applications based on graphene field-effect transistors, *Biosens. and Bioelectron.* 26, 1727–1730 (2010).
- [9] M. D. Stoller, S. Park, Y. Zhu, J. An, R.S. Ruoff, Graphene-based ultracapacitors, *Nano Lett.* 8, 3498–3502 (2008).
- [10] Y. Ding, Y. Wang, L. Su, M. Bellagamba, H. Zhang, Y. Lei, Electrospun Co_3O_4 nanofibers for sensitive and selective glucose detection, *Biosens. Bioelectron.* 26, 542–548 (2010).
- [11] P. You, Z. Liu, Q. Tai, S. Liu, F. Yan, Efficient semitransparent Perovskite solar cells with graphene electrodes, *Adv. Mater.* 27, 323–327 (2015).
- [12] M. E. Suss, S. Porada, X. Sun, P.M. Biesheuvel, J. Yoon, V. Presser, Water desalination via capacitive deionization: what is it and what can we expect from it? *Energy Environ. Sci.* 8, 2296–2319 (2015).
- [13] J. D. Fowler, M.J. Allen, V.C. Tung, Y. Yang, R.B. Kaner, B.H. Weiller, Practical Chemical Sensors from Chemically Derived Graphene, *ACS Nano* 3, 301–306 (2009).
- [14] Q. Xu, H. Xu, J. Chen, Y. Lv, C. Dong, T. S. Sreeprasad, Graphene and graphene oxide: advanced membranes for gas separation and water purification, *Inorg. Chem.* 2, 417–424 (2015).

[15] Y. Jia, *et al.* Defect graphene as a trifunctional catalyst for electrochemical reactions, *Adv. Mater.* 28, 9532–9538 (2016).

[16] S. Gupta, S. B. Carrizosa, B. McDonald, J. Jasinski, N. Dimakis, Graphene-family nanomaterials assembled with cobalt oxides and cobalt nanoparticles as hybrid supercapacitive electrodes and enzymeless glucose detection platforms, *J. Mater. Res.* 32, 301–322 (2016).

[17] M. D. Stoller, S. Park, Y. Zhu, J. An, R. S. Ruoff, Graphene-Based Ultracapacitors, *Nano Lett.* 8, 3498–3502 (2008).

[18] A. Pan, H. B. Wu, L. Yu, X. W. Lou, Template-Free Synthesis of VO₂ Hollow Microspheres with Various Interiors and Their Conversion into V₂O₅ for Lithium-Ion Batteries, *Angew. Chem. Int. Ed.* 125, 2282–2289 (2013).

[19] S. Gupta, M. M. vanMeveren, J. Jasinski, Investigating Electrochemical Properties and Interfacial Processes of Manganese Oxides/Graphene Hybrids as High-Performance Supercapacitor Electrodes, *Int. J. Electrochem. Sci.* 10, 10272–10291 (2015).

[20] J. U. Park, S. Nam, M. S. Lee, C. M. Lieber, Synthesis of monolithic graphene–graphite integrated electronics, *Nature Mater.* 11, 120–125 (2012).

[21] T. Nakajima, A. Mabuchi, R. Hagiwara, A new structure model of graphite oxide, *Carbon*, 26, 357–361 (1988).

[22] W. Schölz, H. P. Z. Boehm, *Zeitschrift für anorganische und allgemeine Chemie*, 369, 327–(1969).

[23] K. Avinash, F. Patolsky, Laser-induced graphene structures: From synthesis and applications to future prospects, *Mater. Today*, 70, 104–136 (2023).

[24] M. F. El-Kady, R. B. Kaner, Direct Laser Writing of Graphene Electronics, *ACS Nano*. 8, 8725–8729 (2014).

[25] J. Lin, Z. Peng, Y. Liu, F. R.-Zepeda, R. Ye, E. L. G. Samuel, M. Jose Yacaman, B. I. Yakobson, J. M. Tour, Laser-induced porous graphene films from commercial polymers, *Nat. Commun.* 5:5714– (2014), *doi: 10.1038/ncomms6714*.

[26] R. Ye, D. K. James, J. M. Tour, Laser-Induced Graphene: From Discovery to Translation, *Adv. Mater.* 31, 1803621– (2019).

[27] A. Tiliakos, C. Ceaus, S. M. Iordache, E. Vasile, I. Stamatina, Morphic Transitions of Nanocarbons via Laser Pyrolysis of Polyimide Films, *J. Anal. Appl. Pyrolysis*. 121, 275–286 (2016).



-
- [28] A. Velasco, Y. K. Ryu, A. Hamada, A. de Andrés, F. Calle, J. Martinez, Laser-Induced Graphene Microsupercapacitors: Structure, Quality, and Performance, *Nanomaterials*, 13(5), 788–796 (2023).
- [29] J. Coelho, R.F. Correia, S. Silvestre, T. Pinheiro, A. C. Marques, M. R. P. Correia, J. V. Pinto, E. Fortunato, R. Martins, Paper-based laser-induced graphene for sustainable and flexible micro-supercapacitor applications, *Microchim. Acta*, 190, 40– (2023).
- [30] H. Wang, Z. Zhao, P. Liu, X. Guo, Laser-Induced Graphene Based Flexible Electronic Devices, *Biosensors*, 12, 55:1–55:21 (2022).
- [31] Y. Xu, Q. Fei, M. Page, G. Zhao, Y. Ling, D. Chen, Z. Yan, Laser-induced graphene for bioelectronics and soft actuators, *Nano Res.* 14, 3033–3050 (2021).
- [32] M. G. Stanford, K. Yang, Y. Chyan, C. Kittrell, J.M. Tour, Laser-Induced Graphene for Flexible and Embeddable Gas Sensors. *ACS Nano*, 13, 3474–3482 (2019).
- [33] B. E. Conway, Transition from "Supercapacitor" to "Battery" Behavior in Electrochemical Energy Storage, *J. Electrochem. Soc.* 138, 1539– (1991).
- [34] S. Gupta, S. B. Carrizosa, Insights into electrode/electrolyte interfacial processes and the effect of nanostructured cobalt oxides loading on graphene-based hybrids by scanning electrochemical microscopy, *Appl. Phys. Lett.* 109, 243903:1–243903:3 (2016).
- [35] S. Gupta, N. Dimakis, Elucidating the effects of oxygen- and nitrogen-containing functional groups in graphene nanomaterials for applied electrochemistry by density functional theory, *J. Appl. Phys.* 130, 084902:1–084902:19 (2016).
- [36] S. Gupta, C. Price, Investigating graphene/conducting polymer hybrid layered composites as pseudocapacitors: Interplay of heterogeneous electron transfer, electric double layers and mechanical stability, *Composites B: Engineering* 105, 46–59 (2016).
- [37] C. Largeot, C. Portet, J. Chimola, P. L. Taberna, Y. Gogotsi, P. Simon, Relation between the Ion Size and Pore Size for an Electric Double-Layer Capacitor, *J. Am. Chem. Soc.* 2008, 130, 2730–2731.
- [38] M. A. Pope, I. A. Aksay, Four-Fold Increase in the Intrinsic Capacitance of Graphene through Functionalization and Lattice Disorder, *J. Phys. Chem. C* 119, 20369–20378 (2015).
- [39] M. Inagaki, H. Konno, O. Tanaike, Carbon materials for electrochemical capacitors, *J. Power Sources* 195, 7880–7903 (2010).
- [40] V. Augustyn, J. Come, M. A. Lowe, J. W. Kim, P.-L. Taberna, S. H. Tolbert, H. D. Abruña, P. Simon, B. Dunn, High-rate electrochemical energy storage through Li^+ intercalation pseudocapacitance, *Nat. Mater.* 12, 518–522 (2013).

-
- [41] J. Cheng, P. Hu, Utilization of the Three-Dimensional Volcano Surface to Understand the Chemistry of Multiphase Systems in Heterogeneous Catalysis, *J. Am. Chem. Soc.* 130, 10868–10869 (2008).
- [42] M. D. Bhatt, H. Kim, G. Kim, Various defects in graphene: a review, *RSC Adv.* 12, 21520–21547 (2022).
- [43] A. Hashimoto, K. Suenaga, A. Gloter, K. Urita, S. Iijima, Direct evidence for atomic defects in graphene layers, *Nature* 430, 870–873 (2004).
- [44] J. -H. Zhong, J. Zhang, X. Jin, J.-Y. Liu, Q. Li, M.-H. Li, W. Cai, D.-Y. Wu, D. Zhan, B. Ren, Quantitative correlation between defect density and heterogeneous electron transfer rate of single layer graphene, *J. Am. Chem. Soc.* 136, 16609–16617 (2014).
- [45] X. Chia, M. Pumera, Characteristics and performance of two-dimensional materials for electrocatalysis, *Nat. Catal.* 1, 909–921 (2018).
- [46] Y. Li, J. Wang, X. Li, D. Geng, M.N. Banis, R. Li, X. Sun, Nitrogen-doped graphene nanosheets as cathode materials with excellent electrocatalytic activity for high-capacity lithium-oxygen batteries, *Electrochem. Commun.* 18, 12–15 (2012).
- [47] A. S. Dobrota, I. A. Pašti, S. V. Mentus, N.V. Skorodumova, A general view on the reactivity of the oxygen-functionalized graphene basal plane, *Phys. Chem. Chem. Phys.* 18, 6580–6586 (2016).
- [48] H. L. Poh, P. Simek, Z. Sofer, I. Tomandl, M. Pumera, Boron and nitrogen doping of graphene via thermal exfoliation of graphite oxide in a BF_3 or NH_3 atmosphere: contrasting properties, *J. Mater. Chem. A* 1, 13146–13153 (2013).
- [49] W. Yuan, Y. Zhou, Y. Li, C. Li, H. Peng, J. Zhang, Z. Liu, L. Dai, G. Shi, The edge- and basal-plane-specific electrochemistry of a single-layer graphene sheet, *Sci. Rep.* 3, 2248– (2013).
- [50] A. Yadav, M. Wehrhold, T.J. Neubert, R. M. Iost, K. Balasubramanian, Fast Electron Transfer Kinetics at an Isolated Graphene Edge Nanoelectrode with and without Nanoparticles: Implications for Sensing Electroactive Species, *ACS Appl. Nano Mater.* 3(12), 11725–11735 (2020).
- [51] Sanju Gupta, Avadh Saxena, Nanocarbon materials: probing the curvature and topology effects using phonon spectra, *J. Raman Spectroscopy* 40, 1127–1137 (2009).
- [52] S. Gupta, A. Saxena (Eds.) in *The Role of Topology in Materials*, Springer Series in Solid-State Sciences, Vol. 189, Springer-Verlag, New York (2018).
- [53] Sanju Gupta, Avadh Saxena, A topological twist on materials science, *MRS Bull.* 39(3), 265–279 (2014).

[54] J. W. Martin, C. deTomas, I. S.-Martinez, M. Kraft, N.A. Marks, Topology of disordered 3D graphene networks, *Phys. Rev. Lett.* 123, 116105:1–116105:4 (2019).

[55] C. E. Banks, T. J. Davies, G.G. Wildgoose, R. G. Compton, Electrocatalysis at graphite and carbon nanotube modified electrodes: edge-plane sites and tube ends are the reactive sites, *Chem. Commun.* 829–841 (2005).

[56] T. J. Davies, M. E. Hyde, R. G. Compton, Nanotrench arrays reveal insight into graphite electrochemistry, *Angew. Chem.* 117, 5251–5256 (2005).

[57] Lai, S. C., Patel, A. N., McKelvey, K. & Unwin, P. R. Definitive evidence for fast electron transfer at pristine basal plane graphite from high-resolution electrochemical imaging. *Angew. Chem.* **124**, 5501–5504 (2012).

[58] C. E. Banks, R. R. Moore, T. J. Davies, R. G. Compton, Investigation of modified basal plane pyrolytic graphite electrodes: definitive evidence for the electrocatalytic properties of the ends of carbon nanotubes, *Chem. Commun.* (2005) 829–841.

[59] C. Tan, J. R. López, J.J. Parks, N.L. Ritzert, D. C. Ralph, H.D. Abruña, Reactivity of Monolayer Chemical Vapor Deposited Graphene Imperfections Studied Using Scanning Electrochemical Microscopy, *ACS Nano* 6, 3070–3079 (2012).

[60] S. Gupta, R. Meek, B. Evans, N. Dimakis, Graphene-based “hybrid” aerogels with carbon nanotubes: Mesoporous network–functionality promoted defect density and electrochemical activity correlations, *J. Appl. Phys.* 124, 124304:1–124304:17 (2018).

[61] H. Taube in *Electron Transfer Reactions of Complex Ions in Solution* (Elsevier, 1970).

[62] T. Pajkossy, D. M. Kolb, Double layer capacitance of the platinum group metals in the double layer region, *Electrochem. Commun.* 9, 1171–1174 (2007).

[63] A. N. Patel, M. G. Collignon, M. A. O’Connell, W. O. Y. Hung, K. McKelvey, J. V. Macpherson, P. R. Unwin, A New View of Electrochemistry at Highly Oriented Pyrolytic Graphite, *J. Am. Chem. Soc.* 134, 49, 20117–20130 (2012).

[64] A. G. Güell, A. S. Cuharuc, Y.-R. Kim, G. Zhang, S. Tan, N. Ebejer, P. R. Unwin, Redox-dependent spatially resolved electrochemistry at graphene and graphite step edges, *ACS Nano*, 9, 3558–3571 (2015).

[65] G. Zhang, A. S. Cuharuc, A. G. Güell, P. R. Unwin, Electrochemistry at highly oriented pyrolytic graphite (HOPG): lower limit for the kinetics of outer-sphere redox processes and general implications for electron transfer models, *Phys. Chem. Chem. Phys.* 17, 11827–11838 (2015).

[66] S. V. Pavlov, R. R. Nazmutdinov, M. V. Fedorov, S. A. Kislenko, Role of graphene edges in the electron transfer kinetics, Insight from theory and molecular modeling, *J. Phys. Chem. C* 123, 6627–6634 (2019).



[67] D. -Q. Liu, M. Kang, D. Perry, C. -H. Chen, G. West, X. Xia, S. Chaudhuri, Z. P. L. Laker, N. R. Wilson, G. N. Meloni, M. M. Melander, R. J. Maurer, P. R. Unwin, Adiabatic *versus* non-adiabatic electron transfer at 2D electrode materials, *Nat. Commun.* 12, 7110– (2021).

[68] C. M. Hill, J. Kim, N. Bodappa, A. J. Bard, Electrochemical nonadiabatic electron transfer via tunneling to solution species through thin insulating films, *J. Am. Chem. Soc.* 139, 6114–6119 (2017).

[69] A. J. Bard, L. R. Faulkner, H. S. White, in *Electrochemical Methods: Fundamentals and Applications*, Third edition, Wiley, Hoboken, NJ (2022).

[70] A. J. Bard, M. V. Mirkin (Eds.), in *Scanning Electrochemical Microscopy*, 2nd Ed. Marcel Dekker, New York (2012).

[71] R. L. McCreery, Advanced Carbon Electrode Materials for Molecular Electrochemistry, *Chem. Rev.* 108, 2646–2687 (2008).

[72] Z. Wang, R. Liu, T. Sun, M. Li, N. Ran, D. Wang, Z. Wang, Revealing Hydrogen Spillover on 1T/2H MoS₂ Heterostructures for an Enhanced Hydrogen Evolution Reaction by Scanning Electrochemical Microscopy, *Anal. Chem.* 96, 19, 7618–7625 (2024).

[73] V. Prabhakaran, R. Kalsar, L. Strange, O. A. Marina, R. Prabhakaran, V. V. Joshi, Understanding Localized Corrosion on Metal Surfaces Using Scanning Electrochemical Cell Impedance Microscopy (SECCIM), *J. Phys. Chem. C* 126, 30, 12519–12526 (2022).

[74] I. A. Pašti, N. V. Skorodumova, S.V. Mentus, Theoretical studies in catalysis and electrocatalysis: from fundamental knowledge to catalyst design, *React. Kinet. Mech. Cat.* 115, 5–32 (2015).

[75] K. Griffiths, C. Dale, J. Hedley, M. D. Kowal, R. B. Kaner, N. Keegan, Laser-scribed graphene presents an opportunity to print a new generation of disposable electrochemical sensors, *Nanoscale*, 6, 13613–13622 (2014).

[76] K. Muzyka, G. Xu, Laser-induced Graphene in Facts, Numbers, and Notes in View of Electroanalytical Applications: A Review, *Electroanal.* 34, 574–589 (2022).

[77] W. Hummers, R. J. Offeman, Preparation of Graphitic Oxide, American Chemical Society, 80, 1339– (1958).

[78] S. Gupta, M. van Meveren, J. Jasinski, Graphene-Based Hybrids with Manganese Oxide Polymorphs as Tailored Interfaces for Electrochemical Energy Storage: Synthesis, Processing, and Properties, *J. Electron. Mater.* 44, 62–78 (2015).

[79] X. Gao, J. Jang, S. Nagase, Hydrazine and Thermal Reduction of Graphene Oxide: Reaction Mechanisms, Product Structures, and Reaction Design, *J. Phys. Chem. C* 114, 832–840 (2010).

-
- [80] S. Park, J. An, R. J. Potts, A. Velamakanni, S. Murali, R. S. Ruoff, Hydrazine-reduction of graphite- and graphene oxide, *Carbon* 49, 3019–3026 (2011).
- [81] I. Sengupta, S. Chakraborty, M. Talukdar, S. K. Pal, S. Chakraborty, Thermal reduction of graphene oxide: How temperature influences purity, *J. Mater. Res.* 33, 4113–4122 (2018).
- [82] S. Gupta, R. Meek, Highly Efficient Thermo-Electrochemical Energy Harvesting from Graphene-Carbon Nanotube ‘Hybrid’ Aerogels, *Appl. Phys. A* 120, 704:1–704:12 (2020).
- [83] S. Gupta, A. Sharits, J. Boeckl, *J. Appl. Phys.* Quantitative morphometry of topological graphene-based aerogels and carbon foams by x-ray micro-computed tomography, 134, 074902:1–074902:12 (2021) [Cover Page].
- [84] W. Nogala, K. Szot, M. Burchardt, F. Roelfs, J. Rogalski, M. Opalloa, G. Wittstock, Feedback mode SECM study of laccase and bilirubin oxidase immobilized in a sol–gel processed silicate film, *Analyst*, 135, 2051–2058 (2010); DOI: 10.1039/c0an00068j.
- [85] C. Kranz, M. Ludwig, H. E. Gaub, W. Schuhmann, Lateral deposition of polypyrrole lines over insulating gaps. Towards the development of polymer-based electronic devices, *Adv. Mater.* 7, 568–571 (1995).
- [86] N. Dimakis, O. Vadodaria, K. Ruiz, S. Gupta, Molybdenum disulfide monolayer electronic structure information as explored using density functional theory and quantum theory of atoms in molecules, *Appl. Surf. Sci.* 555, 149545:1–149545:14 (2021).
- [87] S. Gupta, S.B. Carrizosa, J. Jasinski, N. Dimakis, Charge transfer dynamical processes at graphene-transition metal oxides/electrolyte interface for energy storage: Insights from in-situ Raman spectroelectrochemistry, *AIP Adv.* 8, 065225:1–065225:23 (2018).
- [88] R. Dovesi, V.R. Saunders, C. Roetti, C.M. Zicovich-Wilson, F. Pascale, B. Civalieri, K. Doll, N.M. Harrison, I. J. Bush, P. D’Arco, M. Llunell, M. Causà, Y. Noël, L. Maschio, R. Orlando, A. Erba, M. Rérat, S. Casassa, CRYSTAL17 User’s Manual. Univ. Torino, Torino (2017).
- [89] M. Ernzerhof, G. E. Scuseria, Assessment of the Perdew–Burke–Ernzerhof exchange–correlation functional, *J. Chem. Phys.* 110, 5029–5036 (1999).
- [90] S. Grimme, J. Antony, S. Ehrlich, H. Krieg, A consistent and accurate ab initio parametrization of density functional dispersion correction (DFT-D) for the 94 elements H–Pu, *J. Chem. Phys.* 132, 154104–154118 (2010).
- [91] M. F. Peintinger, D.V. Oliveira, T. Bredow, Consistent Gaussian basis sets of triple-zeta valence with polarization quality for solid-state calculations, *J. Comput. Chem.* 34(6), 451–459 (2013).

- [92] D. V. Oliveira, J. Laun, M. F. Peintinger, T. Bredow, BSSE-correction scheme for consistent gaussian basis sets of double- and triple-zeta valence with polarization quality for solid-state calculations, *J. Comput. Chem.* 40, 2364–2376 (2019).
- [93] H. J. Monkhorst, J. D. Pack, Special points for Brillouin-zone integrations, *Phys. Rev. B*, 13(12), 5188–5192 (1976).
- [94] G. Gilat, L. Raubenheimer, Accurate Numerical Method for Calculating Frequency-Distribution Functions in Solids, *Phys. Rev.* 144, 390– (1966).
- [95] G. Mallia, R. Orlando, C. Roetti, P. Ugliengo, R. Dovesi, *F* center in LiF: A quantum mechanical ab initio investigation of the hyperfine interaction between the unpaired electron at the vacancy and its first seven neighbors, *Phys. Rev. B* 63, 235102:1–235102:7 (2001).
- [96] F. Weigend, R. Ahlrichs, Balanced Basis Sets of Split Valence, Triple Zeta Valence and Quadruple Zeta Valence Quality for H to Rn: Design and Assessment of Accuracy, *Phys. Chem. Chem. Phys.* 7, 3297–3305 (2005).
- [97] A. Erba, K. E. El-Kelany, M. Ferrero, I. Baraille, M. Rérat, Piezoelectricity of SrTiO₃: An *ab initio* description, *Phys. Rev. B* 88, 035102– (2013).
- [98] S. Gupta, M. Narajczyk, M. Sawczak, J. B. Jasinski, R. Bogdanowicz, S. Yang, Flexible MXene/Laser-Induced Porous Graphene Asymmetric Supercapacitors: Enhanced Energy Density of Lateral and Sandwich Architectures Under Different Electrolytes, *Small* 21, (2025); <https://doi.org/10.1002/sml.202502297>.
- [99] Z. Zhang, H. Zhu, W. Zhang, Z. Zhang, J. Lu, K. Xu, Y. Liu, V. Saetang, A review of laser-induced graphene: From experimental and theoretical fabrication processes to emerging applications, *Carbon* 214, 118356 (2023).
- [100] T.-S. D. Le, H.-P. Phan, S. Kwon, S. Park, Y. Jung, J. Min, *et. al.*, Recent Advances in Laser-Induced Graphene: Mechanism, Fabrication, Properties, and Applications in Flexible Electronics, *Adv. Func. Mater.* 32(48), 2205158 (2022).
- [101] J. Liu, H. Ji, X. Lv, C. Zeng, H. Li, F. Li, B. Qu, F. Cui, Laser-induced graphene (LIG)-driven medical sensors for health monitoring and diseases diagnosis, *Microchim. Acta* 189, 54:1–54:14 (2022).
- [102] T.-R. Cui, D. Li, T. Hirtz, W.-C. Shao, Z.B. Zhou, S.-R. Ji, ..., T. -L. Ren, Laser-Induced Graphene for Multifunctional and Intelligent Wearable Systems: For Health Care and Human–Computer Interaction, *Appl. Sci.* 13(8), 4688:1–4688:23 (2023).
- [103] M. I. Nathan, J. E. Smith Jr., K. N. Tu, Raman spectra of glassy carbon, *J. Appl. Phys.* 45, 2370–2375 (1974).



- [104] Lucchese, M. M.; Stavale, F.; Ferreira, E. H.; Vilane, C.; Moutinho, M. V. O.; Capaz, R. B.; Achete, C. A.; Jorio, A. Quantifying ion-induced defects and Raman relaxation length in graphene, *Carbon*, 48, 1592–1597 (2010).
- [105] L. G. Cançado, A. Jorio, E. H. Martins Ferreira, F. Stavale, C. A. Achete, R. B. Capaz, M. V. O. Moutinho, A. Lombardo, T. S. Kulmala, A. C. Ferrari, Quantifying Defects in Graphene *via* Raman Spectroscopy at Different Excitation Energies, *Nano Lett.* 11, 3190–3196 (2011).
- [106] A. Das, S. Pisana, B. Chakraborty, S. Piscanec, S. K. Saha, U.V. Waghmare, K. S. Novoselov, H. R. Krishnamurthy, A. K. Geim, A. C. Ferrari, A. K. Sood, Monitoring dopants by Raman scattering in an electrochemically top-gated graphene transistor, *Nat. Nanotech.* 3, 210–215 (2008).
- [107] D. A. C. Brownson, D. K. Kampouris, C. E. Banks, Graphene electrochemistry: fundamental concepts through to prominent applications, *Chem. Soc. Rev.* 41, 6944–6976 (2012).
- [108] K. Sathiyar, C. Gao, T. Wada, P. Mukherjee, K. Seenivasan, T. Taniike, Structure-Driven Performance Enhancement in Palladium–Graphene Oxide Catalysts for Electrochemical Hydrogen Evolution, *Materials* 17(21), 5296– (2024).
- [109] R. M.-Hincapié, J. Wegner, M. U. Anwar, A. R.-Khan, S. Franzka, S. Kleszczynski, V. Čolić, The determination of the electrochemically active surface area and its effects on the electrocatalytic properties of structured nickel electrodes produced by additive manufacturing, *Electrochim. Acta* 476, 143663– (2024).
- [110] D. Menshikau, I. Streeter, R. G. Compton, Influence of electrode roughness on cyclic voltammetry, *J. Phys. Chem. C* 112, 14428– (2008).
- [111] J. Chen, Y. Han, X. Kong, X. Deng, H. J. Park, Y. Guo, S. Jin, Z. Qi, Z. Lee, Z. Qiao, R. S. Ruoff, H. Ji, The origin of improved electrical double-layer capacitance by inclusion of topological defects and dopants in graphene for supercapacitors, *Angew. Chem.* 128, 14026–14031 (2016).
- [112] A. J. Pak, E. Paek, G. S. Hwang, Tailoring the performance of graphene-based supercapacitors using topological defects: A theoretical assessment, *Carbon*, 68, 734–741 (2014).
- [113] S.C.B. Oliveira, A. M. Oliveira-Brett, Voltammetric and electrochemical impedance spectroscopy characterization of a cathodic and anodic pre-treated boron doped diamond electrode, *Electrochim. Acta* 55, 4599–4605 (2010).
- [114] S. Kochowski, K. Nitsch, Description of the frequency behavior of metal–SiO₂–GaAs structure characteristics by electrical equivalent circuit with constant phase element, *Thin Solid Films* 415 (1–2) (2002) 133–137.
- [115] B. Hirschorn, M. E. Orazem, B. Tribollet, V. Vivier, I. Frateur, M. Musiani, Constant-phase-element behavior caused by resistivity distributions in films I. Theory. *J. Electrochim. Soc.* 2010, 157, C452–C457.

-
- [116] G.J. Brug, A.L.G. van den Eeden, M. S.-Rehbach, J.H. Sluyters, The analysis of electrode impedances complicated by the presence of a constant phase element, *J. Electroanal. Chem. Interfacial Electrochem.* 176 (1), 275–295 (1984).
- [117] H. Zanin, P. W. May, D.J. Fermin, D. Plana, S. M. C. Vieira, W.I. Milne, E.J. Corat, Porous boron-doped diamond/carbon nanotube electrodes, *ACS Appl. Mater. Interfaces* 6, 990–995 (2014).
- [118] M. E. Orazem, N. Pébère, B. Tribollet, Enhanced graphical representation of electrochemical impedance data, *J. Electrochem. Soc.* 2006, 153, B129.
- [119] C. L. Bentley, M. Kang, P. R. Unwin, Nanoscale surface structure-activity in electrochemistry and electrocatalysis, *J. Am. Chem. Soc.* 141, 2179–2193 (2018).
- [120] P. Chen, R. L. McCreery, Control of electron transfer kinetics at glassy carbon electrodes by specific surface modification, *Anal. Chem.* 68, 3958–3965 (1996).
- [121] A. Ambrosi, C. K. Chua, A. Bonanni, M. Pumera, Electrochemistry of Graphene and Related Materials, *Chem. Rev.* 114, 7150–7188 (2014).
- [122] Y. Yu, K. Zhang, H. Parks, M. Babar, S. Carr, I. M. Craig, ..., D. K. Bediako, Tunable angle-dependent electrochemistry at twisted bilayer graphene with moiré flat bands, *Nat. Chem.* 14, 267–273 (2022).
- [123] R. S. Nicholson, Theory and application of cyclic voltammetry for measurement of electrode reaction kinetics, *Anal. Chem.* 37, 1351–1355 (1965).
- [124] I. Lavagnini, R. Auliochia, F. Magno, An extended method for the practical evaluation of the standard rate constant from cyclic voltammetric data, *Electroanalysis*, 16, 505–506 (2004).
- [125] D. Nkosi, J. Pillay, K. I. Ozoemena, K. Nouneh, M. Oyama, Heterogeneous electron transfer kinetics and electrocatalytic behaviour of mixed self-assembled ferrocenes and SWCNT layers, *Phys. Chem. Chem. Phys.* 12, 604–613 (2010).
- [126] J. N. Soderberg, A.C. Co, A.H.C. Sirk, V.I. Birss, Impact of porous electrode properties on the electrochemical transfer coefficient, *J. Phys. Chem. B* 110, 10401–10410 (2006).
- [127] M. M. Melander, Grand canonical rate theory for electrochemical and electrocatalytic systems I: general formulation and proton-coupled electron transfer reactions, *J. Electrochem. Soc.* 167, 116518 (2020).
- [128] R. A. Marcus, Chemical and electrochemical electron-transfer theory, *Annu. Rev. Phys. Chem.* 15, 155–196 (1964).
- [129] R. Marcus, On the Theory of Oxidation-Reduction Reactions Involving Electron Transfer. I. *The Journal of Chemical Physics* 24(5), 966–978 (1956).



[130] A. Eftekhari, Carbon nanowalls as material for electrochemical transducers, *Appl. Phys. Lett.* 96, 126102–126104 (2009).

[131] E. Luaïs, M. Boujtita, A. Gohier, A. Tailleux, S. Casimirius, M. A. Djouadi, A. Granier, P. Y. Tessier, Carbon nanowalls as material for electrochemical transducers, *Appl. Phys. Lett.* 95, 014104–014106 (2009).

[132] R. Cornut, C. Lefrou, New analytical approximations for negative feedback currents with a microdisk SECM tip, *J. Electroanal. Chem.* 604, 91–100 (2008).

[133] R. R. Nazmutdinov, M. D. Bronshtein, E. Santos, Electron transfer across the graphene electrode/solution interface: interplay between different kinetic regimes, *J. Phys. Chem. C* 123, 12346–12354 (2019).

[134] E. Vaughan, C. Larrigy, M. BurkeLabrini Sygellou, A. J. Quinn, C. Galiotis, D. Iacopino, Visible Laser Scribing Fabrication of Porous Graphitic Carbon Electrodes: Morphologies, Electrochemical Properties, and Applications as Disposable Sensor Platforms, *ACS Appl. Electron. Mater.* 2(10), 3279–3288 (2020).

[135] T. J. Davies, C.E. Banks, R.G. Compton, Voltammetry at spatially heterogeneous electrodes, *J. Sol. Stat. Electrochem.* 9, 797–808 (2005).

[136] A. Jorio, M.M. Lucchese, F. Stavale, E.H. Ferreira, M.V. Moutinho, R.B. Capaz, C.A. Achete, Raman study of ion-induced defects in N-layer graphene, *J. Phys.: Condens. Matter*, 22, 334204 (2010).

[137] E. Paek, A. J. Pak, K. E. Kweon, G.S. Hwang, On the Origin of the Enhanced Supercapacitor Performance of Nitrogen-Doped Graphene, *J. Phys. Chem. C*, 117, 5610–5616 (2013).

[138] X. Ning, Y. Li, J. Ming, Q. Wang, H. Wang, Y. Cao, F. Peng, Y. Yang, H. Yu, Electronic synergism of pyridinic- and graphitic-nitrogen on N-doped carbons for the oxygen reduction reaction, *Chem. Sci.* 10, 1589–1596 (2019).

[139] E. Frackowiak, G. Lota, J. Machnikowski, C. V.- Guterl, F. Beguin, Optimization of supercapacitors using carbons with controlled nanotexture and nitrogen content, *Electrochim. Acta* 51, 2209–2214 (2006).

[140] S. A. Kislenko, F. Juarez, F. D.- Flores, W. Schmickler, R. R. Nazmutdinov, Tuning the rate of an outer-sphere electron transfer by changing the electronic structure of carbon nanotubes, *J. Electroanal. Chem.* 847, 113186– (2019).

[141] M. Seredych, D. H.- Jurcakova, G. Q. Lu, T. J. Bandoz, Surface functional groups of carbons and the effects of their chemical character, density and accessibility to ions on electrochemical performance, *Carbon*, 46, 1475–1488 (2008).

[142] O. J. Wahab, E. Daviddi, B. Xin, P. Z. Sun, E. Griffin, A. W. Colburn, D. Barry, M. Yagmurcukardes, F. M. Peeters, A. K. Geim, M. Lozada-Hidalgo, P. R. Unwin, Proton transport through nanoscale corrugations in two-dimensional crystals, *Nature* 620, 782–786 (2023).

[143] V. A. Kislenko, S. V. Pavlov, S. A. Kislenko, Influence of defects in graphene on electron transfer kinetics: The role of the surface electronic structure, *Electrochimica Acta* 341, 136011–(2020).

[144] H. Gerischer, in *Physical Chemistry: An Advanced Treatise*; H. Eyring, D. Henderson, W. Jost (Eds.) Academic Press Inc. Vol. 9A, New York (1970).

[145] S. Schmickler, in *Interfacial Electrochemistry*, 2nd Ed. pp. 167 (2010).

[146] R. L. McCreery, M. T. McDermott, Comment on Electrochemical Kinetics at Ordered Graphite Electrodes, *Anal. Chem.* 84, 2602– (2012).

[147] Z. Hu, J. Vatamanu, O. Borodin, D. Bedrov, A molecular dynamics simulation study of the electric double layer and capacitance of [BMIM][PF₆] and [BMIM][BF₄] room temperature ionic liquids near charged surfaces, *Phys. Chem. Chem. Phys.*, 15, 14234–14247 (2013).

[148] J. Ma, D. Alfe, A. Michaelides, E. Wang, Stone-Wales defects in graphene and other planar sp²-bonded materials, *Phys. Rev. B* 80, 33407– (2009).

[149] S. Gupta, B. Aberg, S. B. Carrizosa, N. Dimakis, Vanadium Pentoxide Nanobelt-Reduced Graphene Oxide Nanosheet Composites as High-Performance Pseudocapacitive Electrodes: ac Impedance Spectroscopy Data Modeling and Theoretical Calculations, *Materials* 9(8), 615–635 (2016).

[150] G. M. Yang, H. Z. Zhang, X. F. Fan, W. T. Zheng, Density Functional Theory Calculations for the Quantum Capacitance Performance of Graphene-Based Electrode Material, *J. Phys. Chem. C*, 119, 6464–6470 (2015).

[151] I. Heller, J. Kong, K. A. Williams, C. Dekker, S. G. Lemay, Electrochemistry at Single-Walled Carbon Nanotubes: The Role of Band Structure and Quantum Capacitance, *Am. Chem. Soc.* 128, 7353– (2006).

[152] J. Xia, F. Chen, J. Li, N. Tao, Measurement of the quantum capacitance of graphene, *Nat. Nanotechnol.* 4, 505–509 (2009).

[153] I. Heller, J. Kong, K. A. Williams, C. Dekker, S. G. Lemay, Electrochemistry at single-walled carbon nanotubes: the role of band structure and quantum capacitance, *J. Am. Chem. Soc.* 128, 7353–7359 (2006).

[154] X. Mao, F. Guo, E. H. Yan, G. C. Rutledge, T. A. Hatton, Remarkably high heterogeneous electron transfer activity of carbon-nanotube-supported reduced graphene oxide, *Chem. Mater.* 28, 7422–7432 (2016).



[155] W.M. Haynes, in *CRC Handbook of Chemistry and Physics*, CRC Press, 2017.

[156] A. G. Güell, N. Ebejer, M. E. Snowden, J. V. Macpherson, P. R. Unwin, Structural correlations in heterogeneous electron transfer at monolayer and multilayer graphene electrodes, *J. Am. Chem. Soc.* **134**, 7258–7261 (2012).

[157] C. Lefrou, R. Cornut, Analytical expressions for quantitative scanning electrochemical microscopy (SECM), *Chem. Phys. Chem.* **11**, 547–556 (2010).

[158] J. L. Amphlett, G. Denault, Scanning electrochemical microscopy (SECM): An investigation of the effects of tip geometry on amperometric tip response, *J. Phys. Chem. B* **102**, 9946–9951 (1998).